



Article

Analysis of Torque Characteristics in Dual Three-Phase PMSMs with Asymmetric IPM Rotors

Shensheng Wang ¹, Zi-Qiang Zhu ^{1,*}, Yang Xiao ² and Dawei Liang ¹

- School of Electrical and Electronic Engineering, University of Sheffield, Sheffield S1 3JD, UK; seueelab_wss@163.com (S.W.); d.liang@sheffield.ac.uk (D.L.)
- ² School of Engineering, University of Leicester, Leicester, LE1 7RH, UK; yx224@leicester.ac.uk
- * Correspondence: z.q.zhu@sheffield.ac.uk

Abstract

In this paper, the effects of asymmetric interior permanent magnet (AIPM) rotors on the torque characteristics in dual three-phase (DTP) permanent magnet synchronous machines (PMSMs) are investigated. The electromagnetic performances of DTP PMSMs with symmetrical and asymmetric IPM rotors are compared, including air-gap flux density, back EMF, cogging torque, torque, loss, and efficiency. It is found that in DTP PMSMs, the AIPM rotor can achieve significant torque improvement under both healthy and single three-phase open-circuit conditions. It is also found that performance enhancement in AIPM DTP machines is more remarkable across the constant torque region, particularly at high-load conditions, than in the constant power region, compared with the symmetrical IPM counterpart. A prototype is fabricated and tested to verify theoretical analyses.

Keywords: asymmetric interior permanent magnet rotor; dual three-phase; interior permanent magnet rotor; permanent magnet synchronous machine

1. Introduction

In recent years, multi-phase permanent magnet synchronous machines (PMSMs) have been widely researched due to their advantages, including high power/torque density, high efficiency, reduced current/power rating per phase, and enhanced fault tolerance capability [1–3]. Compared with other types of multi-phase PMSMs, dual three-phase (DTP) PMSMs have attracted more attention, since commercial standard three-phase inverters can be employed directly and the control strategy is, relatively, easier in DTP PMSMs [4–13]. In addition, considering the independent two winding sets in DTP PMSMs, the faults in one three-phase winding set will not lead to the full loss of torque output, and the fault-tolerant control strategy in DTP PMSMs is also easier than in other multi-phase PMSMs [4,5].

Regardless of winding configuration, the rotors in DTP PMSMs can be generally classified into surface-mounted permanent magnet (SPM) rotors [6–9] and interior permanent magnet (IPM) rotors [10–13]. Compared with IPM rotors, the PMs in SPM rotors are placed closer to the air-gap, and the flux leakages in SPM rotors are smaller. However, the d- and q-axis inductances are almost the same in SPM rotors. Thus, SPM rotors cannot produce reluctance torque. In IPM rotors, the existence of rotor saliency makes it possible to utilize both PM torque and reluctance torque at the same time [11,12]. What is more, the PMs in IPM rotors are buried in rotor cores, which means that there is no need to consider glass/carbon fiber banding under high speed. Thus, IPM rotors are especially suitable for variable-speed applications, such as electric vehicles [12,13].



Academic Editor: Adolfo Dannier

Received: 22 August 2025 Revised: 14 October 2025 Accepted: 15 October 2025 Published: 17 October 2025

Citation: Wang, S.; Zhu, Z.-Q.; Xiao, Y.; Liang, D. Analysis of Torque Characteristics in Dual Three-Phase PMSMs with Asymmetric IPM Rotors. *Energies* **2025**, *18*, 5477. https://doi.org/10.3390/en18205477

Copyright: © 2025 by the authors. Licensee MDPI, Basel, Switzerland. This article is an open access article distributed under the terms and conditions of the Creative Commons Attribution (CC BY) license (https://creativecommons.org/licenses/by/4.0/).

Energies **2025**, 18, 5477

To further improve the torque performances of PMSMs with IPM rotors, asymmetric IPM (AIPM) rotor topologies have been investigated in some papers [14–20]. In [14], the adoption of assisted flux barriers in V-type IPM machines displaces the axis of reluctance torques, which increases the average torque. In [15–18], the asymmetric magnet and flux barrier are optimized synchronously in PM-assisted synchronous reluctance machines. The axes of the PM and reluctance torque components can also be shifted closer by combining different types of rotor topologies [19–24]. For example, the asymmetric inset SPM rotor structures introduced in [19,20] can be seen as compositions of the SPM rotor and reluctance rotor. In addition, besides in a circumferential direction [19,20], the SPM rotor and reluctance rotor can also be composed together in an axial direction [21,22]. Furthermore, besides the combination of SPM and reluctance rotors, asymmetric rotors can also be combined by SPM and IPM rotors [23], or by different types of IPM rotors (e.g., I-type and spoke-type PMs in [24] and V-type and spoke-type PMs in [25]). All of these asymmetric rotor designs can shift the reluctance torque axis closer to the PM torque axis in PMSMs, and thus, the utilization ratios of PM and reluctance torque components can be improved simultaneously [26–29].

Compared with conventional single three-phase (STP) PMSMs, DTP PMSMs have inherently higher average torque and reduced torque harmonics [10]. However, existing papers only focus on the effects of AIPM rotors in the conventional single three-phase (STP) winding configuration [30]. The effects of AIPM rotors on the electromagnetic characteristics in DTP PMSMs have not been analyzed. Therefore, this paper aims to fill this gap by investigating and comparing the influences of symmetrical and asymmetric IPM rotors on electromagnetic performances in DTP PMSMs. Considering that a single three-phase open-circuit (OC) is a special but important operation condition for DTP PMSMs, both healthy and single three-phase OC conditions are considered.

This paper is organized as follows. In Section 2, the topologies and working principles of the analyzed DTP PMSMs with IPM and AIPM rotors are described. The electromagnetic performances of the DTP PMSMs with IPM and AIPM rotors are compared under healthy conditions in Section 3, and under single three-phase OC conditions in Section 4. In Section 5, a prototype of the DTP PMSM with an AIPM rotor is manufactured and tested to verify the analyses. Finally, the conclusions are drawn in Section 6.

2. Machine Configuration and Operation Principle

In this paper, the effects of AIPM rotors on DTP PMSMs are investigated based on the Toyota Prius 2010 machine, and the results are compared with those obtained with the original symmetrical IPM rotor. Considering that the original Toyota Prius 2010 machine is equipped with STP windings, the DTP winding configuration for Toyota Prius 2010 machine will also be introduced in this section.

2.1. Machine Configuration

In the Toyota Prius 2010 machine, the slot/pole number combination is 48-slot/8-pole, and the original armature windings are single-layer short-pitched STP windings [31]. Compared with the STP winding configuration, the DTP winding configuration with 30° phase shift can improve average torque and reduce torque ripples inherently. Hence, to enhance the torque performance of the original Toyota Prius 2010 machine, two DTP winding configurations are proposed and compared in [32]. In this paper, the single-layer full-pitched DTP winding configuration is selected for further analyses due to its advantages, which include enhanced average torque capability and easier manufacture. The winding arrangement and the coil electromotive force (EMF) phasor diagram of the

Energies 2025, 18, 5477 3 of 28

single-layer full-pitched DTP windings are shown in Figure 1a,b, respectively. The phase shift angle (30°) can be observed clearly in Figure 1b.

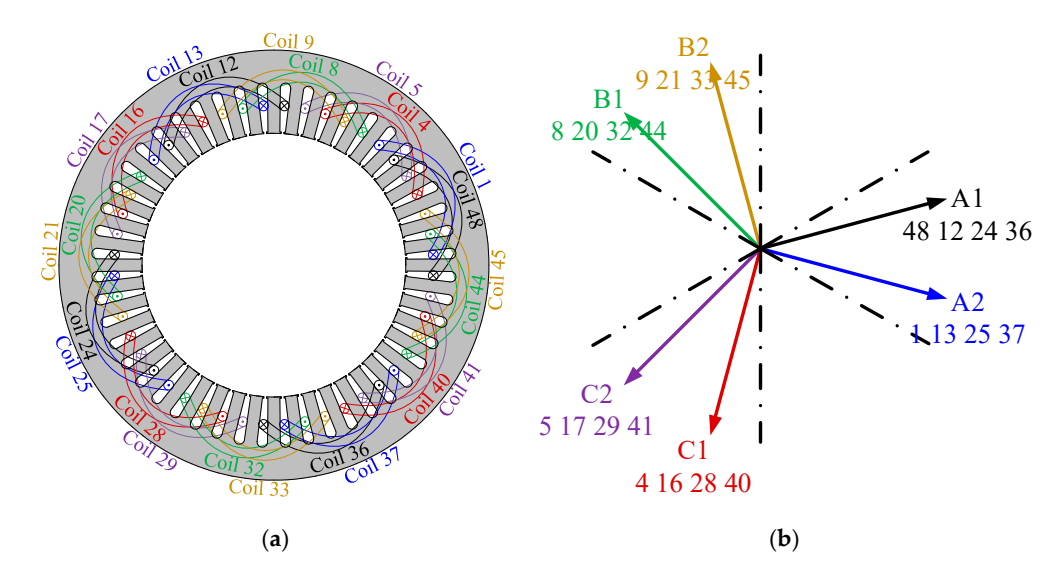


Figure 1. Winding configuration of DTP windings in Toyota Prius 2010 machine. (a) Winding arrangement. (b) Phase EMF phasor diagram.

The AIPM rotor design analyzed in this paper is firstly proposed in [30], based on the Toyota Prius 2010 machine for STP stator windings, which features skewed V-type PMs and a flux barrier outside the PMs. The cross-sections of the benchmark DTP PMSMs with the original symmetrical IPM rotor (designated as the IPM rotor in the rest of the paper) and the AIPM rotor are illustrated in Figure 2a,b, respectively. The detailed geometric dimensions of the Toyota Prius 2010 machine, including the stator and the IPM rotor and the AIPM rotor can be found from [31,33,34], respectively, and some key geometric parameters are listed in Table 1.

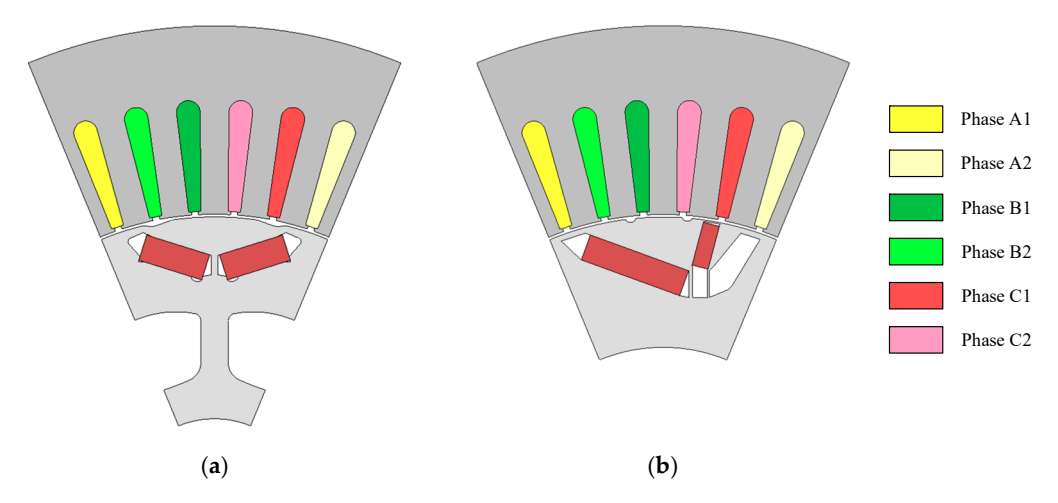


Figure 2. Cross-sections of DTP PMSMs with IPM and AIPM rotors. (a) IPM. (b) AIPM.

2.2. Theoretical Analyses

As shown in Figure 1b, for the PMSM with conventional STP windings, the windings belonging to Phases A1 and A2 are fed with identical currents, and thus, the winding factor for the fundament torque harmonic can be calculated as $\cos(15^\circ) = 0.966$. However, for the PMSM with DTP windings, the windings belonging to Phases A1 and A2 are fed with currents with a phase shift angle (30°), and thus, the winding factor for the fundament torque harmonic is 1. Furthermore, based on the winding configuration and

Energies 2025, 18, 5477 4 of 28

the currents with phase shift angles, it can be calculated that the fundamental flux linkage can be enhanced by 3.5%, and the sixth torque harmonics can be eliminated by using DTP windings [32]. In other words, no matter if using the IPM rotor or AIPM rotor, the average torque improvement and torque ripple reductions can be expected. However, the actual on-load torque performance is closely related to the magnetic saturation level in the machine, especially in PMSMs with IPM rotors. The magnetic cross-saturation in PM machines cannot be taken into account when calculating winding factors, and hence, FE analyses should be carried out to demonstrate how AIPM rotors affect the on-load torque performance in DTP PMSMs.

Table 1. Main design specifications of benchmark PMSM.

Parameters	Values	
Stator		
Stator OD, mm	264	
Stator ID, mm	161.9	
Stack length, mm	50.8	
Slot depth, mm	30.9	
Slot opening, mm	1.88	
Stator material	Silicon steel sheet (50H250)	
IPM rotor		
Rotor OD, mm	160.4	
Rotor ID, mm	51	
Stack length, mm	50.8	
Rotor material	Silicon steel sheet (50H250)	
PM length, mm	17.88	
PM thickness, mm	7.16	
Total PM volume, mm ³	104,055.31	
PM material	NdFeB	
PM remanence, T	1.2	
PM relative permeability	1.05	
AIPM rotor		
Rotor OD, mm	160.4	
Rotor ID, mm	90	
Stack length, mm 50.8		
Rotor material	Silicon steel sheet (50H250)	
Large PM length, mm 28.3		
Large PM thickness, mm	7.2	
Small PM length, mm		
Small PM thickness, mm	4.36	
Total PM volume, mm ³	104,055.31	
PM material	NdFeB	
PM remanence, T	1.2	
PM relative permeability	1.05	

2.3. Operation Principle

Although the winding configurations in DTP PMSMs are different from those in their STP counterparts, the output torques of DTP and STP PMSMs are both composed of PM and reluctance torque components. Thus, the operation principle of AIPM rotors in DTP PMSMs is identical to that in STP PMSMs. The PM torque component is produced by the interaction between armature windings and the PM magnetic field, while reluctance torque is produced due to the rotor saliency. Compared with the IPM rotor, the AIPM rotor shifts the axis of the PM magnetic field and changes the location of rotor saliency simultaneously.

Energies **2025**, 18, 5477 5 of 28

Thus, when using the AIPM rotor in PMSMs, the optimal current advancing angles for the maximum PM and reluctance torque components are no longer the same as those obtained using the IPM rotor. With appropriate AIPM rotor designs, the optimal current advancing angles for maximum PM and reluctance torque components can be much closer to each other. Thus, both PM and reluctance torque components can be utilized more effectively with the same current advancing angle. To further illustrate the difference between the torque components in PMSMs with IPM and AIPM rotors, the torque components versus current advancing angle characteristics in the PMSMs with different rotors are plotted in Figure 3.

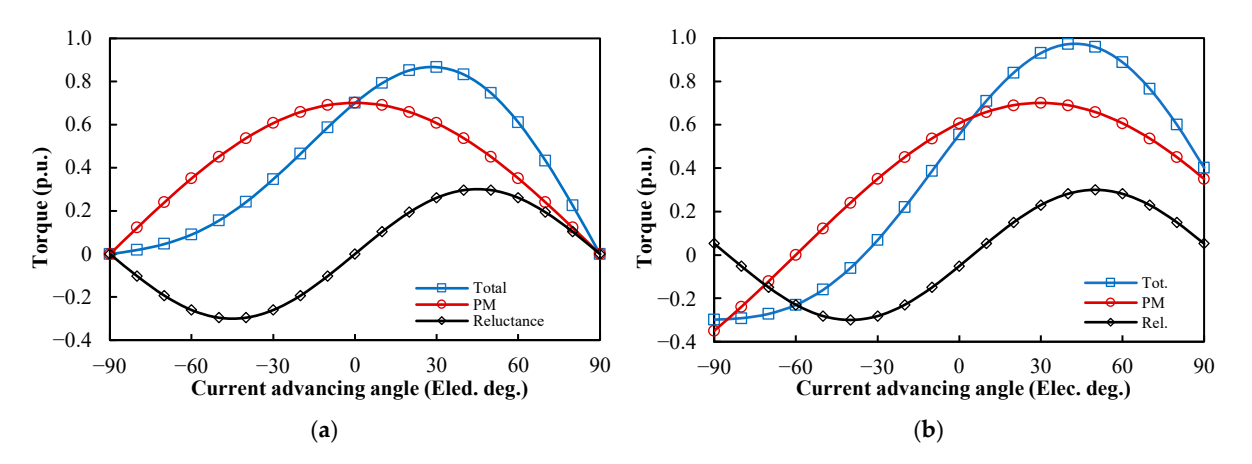


Figure 3. Torque components of PMSMs with different rotors. (a) IPM. (b) AIPM.

Overall, compared with the IPM counterpart, the magnetic field shifting (MFS) effect caused by the AIPM rotor makes it possible to produce higher average torque. In the analyzed AIPM rotor, as shown in Figure 2b, the different sizes of two interior PMs and the extra flux barrier can make the MFS effect even more evident.

3. Comparison of Electromagnetic Performance of DTP PMSMs with IPM and AIPM Rotors Under Healthy Condition

In this section, the electromagnetic performances of the benchmark DTP PMSMs with IPM and AIPM rotors are compared, including comparisons of air-gap flux density, back EMF, cogging torque, torque, loss, and efficiency. It should be mentioned that all the analyses presented below are based on the results obtained from JMAG-Designer by using 2-dimensional (2D) finite element (FE) method.

3.1. Open-Circuit Characteristics

The flux line distributions of the DTP PMSMs with IPM and AIPM rotors under OC conditions are firstly calculated and compared, as shown in Figure 4. As can be seen, due to the middle-side small magnet and the outside flux barrier in one AIPM rotor pole, closed flux lines can be observed. The waveforms and spectra of the radial flux densities along air-gaps under this condition are shown in Figure 5a,b. In Figure 5a, the fluctuations can be explained by the asymmetric rotor layout and the closed flux lines in one AIPM rotor pole. In Figure 5b, it can be clearly seen that the AIPM rotor has a higher fundamental component, which can be attributed to the flux-focusing effect caused by the flux barrier in the AIPM rotor. However, the AIPM machine also shows more harmonic contents compared with its IPM counterpart, which may result in larger eddy current loss in the AIPM machine. Hence, the flux density distributions of the benchmark PMSMs under OC conditions suggest that the loss and efficiency of the DTP PMSMs with IPM and AIPM rotors need more attention in the following analyses.

Energies 2025, 18, 5477 6 of 28

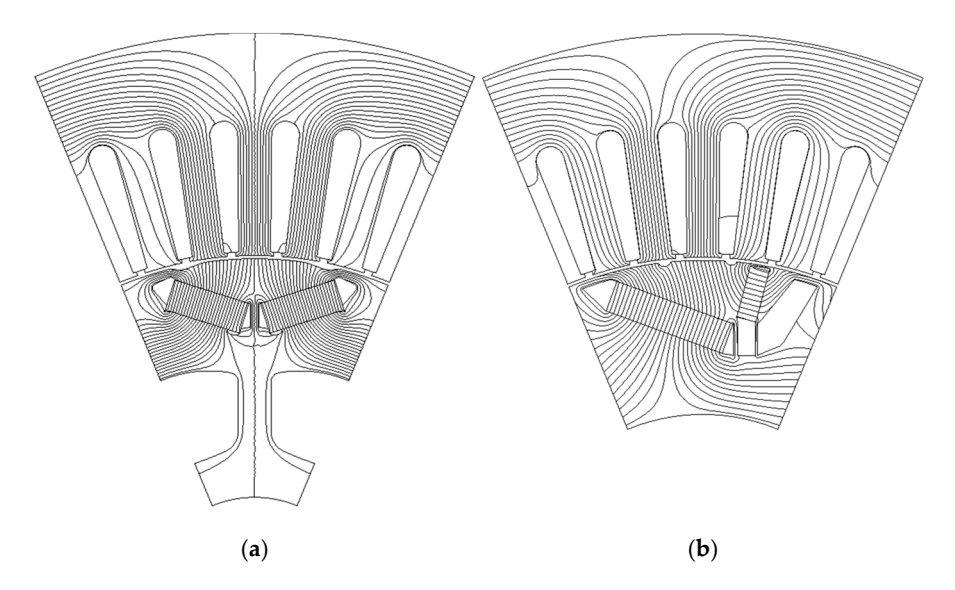


Figure 4. Flux line distributions of DTP PMSMs with different rotors under open circuit conditions. (a) IPM. (b) AIPM.

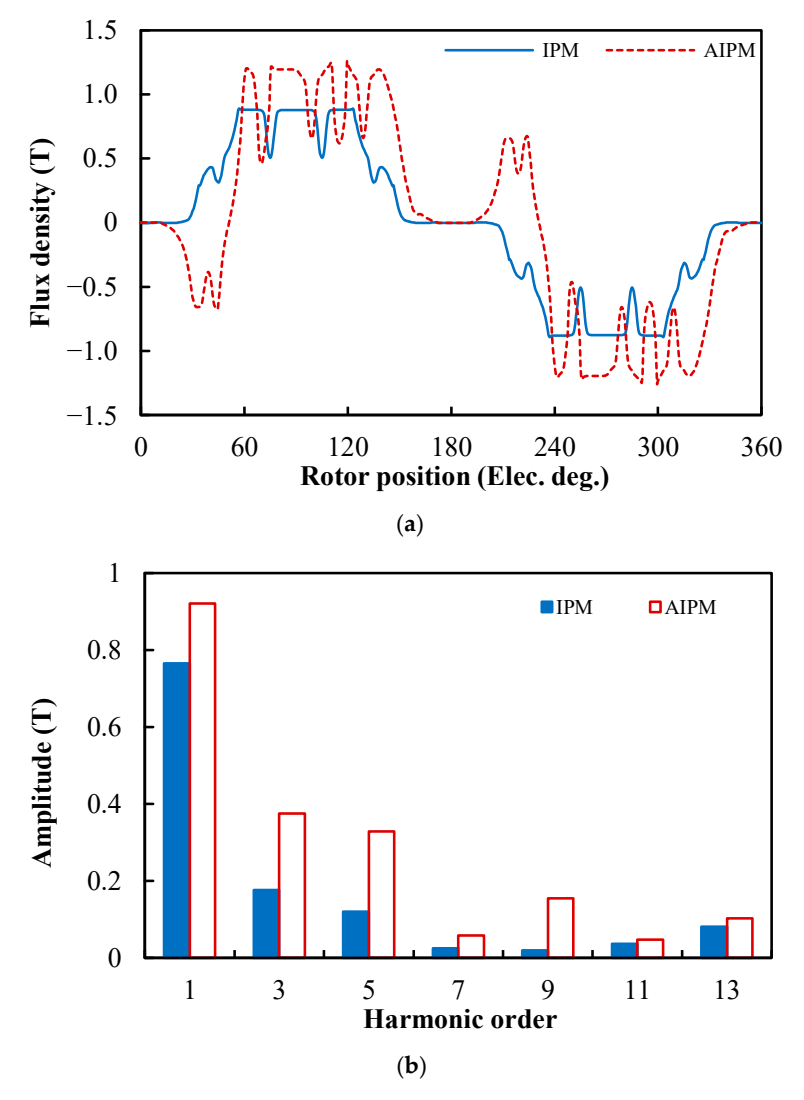


Figure 5. Air-gap flux densities of DTP PMSMs with different rotors under open circuit conditions. (a) Waveforms. (b) Spectra (amplitude).

Energies 2025, 18, 5477 7 of 28

In the DTP PMSMs with IPM and AIPM rotors, assuming rotor speed is 200 rpm, the waveforms and spectra of phase back electromotive forces (EMFs) of Phases A1 and A2 are shown in Figure 6. In Figure 6b, it can be seen that similarly to the OC air-gap flux density, the amplitude of the fundamental back EMF in the AIPM machine is higher than that in the IPM machine.

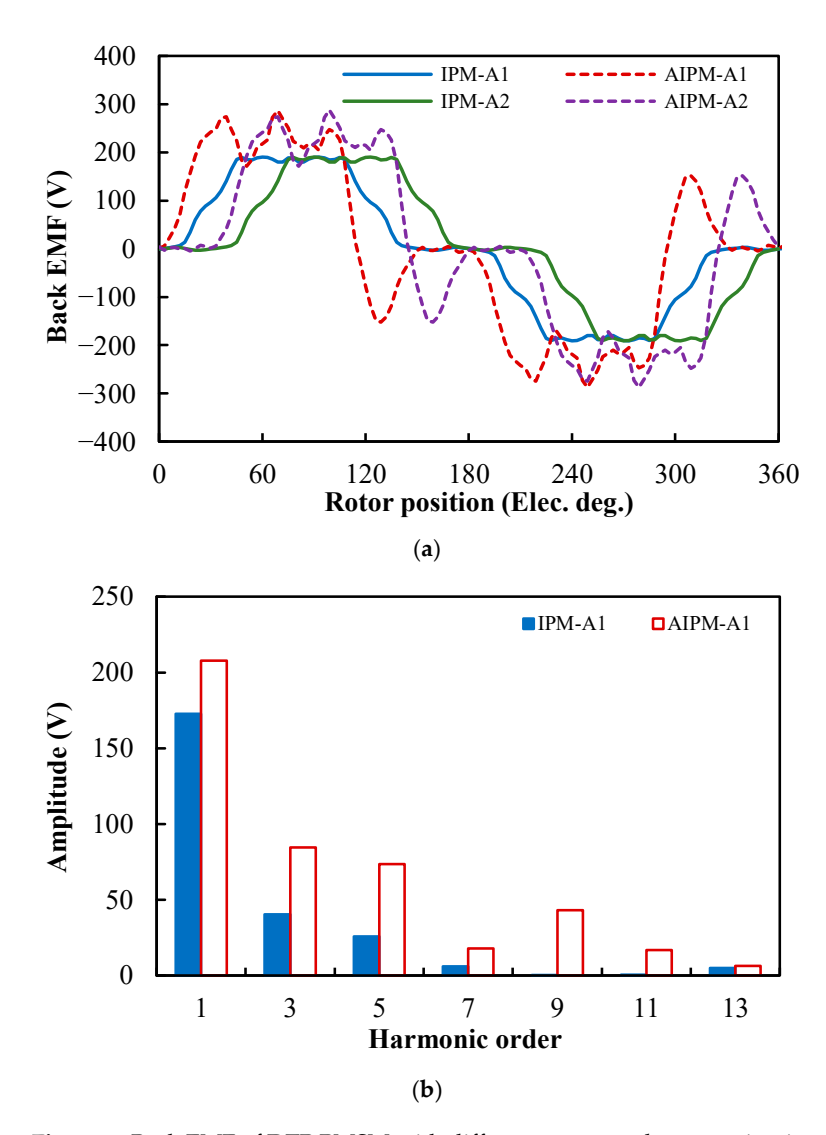


Figure 6. Back EMF of DTP PMSM with different rotors under open circuit conditions. (a) Waveforms. (b) Spectra (amplitude).

For the DTP PMSMs with IPM and AIPM rotors, the waveforms and spectra of the cogging torques are given in Figure 7a,b. Due to the same slot/pole number combination, the fundamental orders of cogging torque in the IPM and AIPM machines are exactly the same, which is 48 in mechanical angle (the smallest common multiple between slot number, 48, and pole number, 8) and 12 in electric angle, but the amplitudes of the same harmonic order are different in the IPM and AIPM machines. In the analyzed DTP PMSMs, the cogging torque produced by the AIPM rotor is much larger than that produced by the IPM rotor.

3.2. Torque Characteristics

In this section, the torque characteristics of the DTP PMSMs with IPM and AIPM rotors are first compared under the full load. In the Toyota Prius 2010 machine, the phase current amplitude under the full load is 236 A, and in the benchmark DTP PMSMs, due to

Energies 2025, 18, 5477 8 of 28

different winding configurations, the phase current amplitude for the full load is 118 A. In the DTP PMSMs with IPM and AIPM rotors, the variations in average torque with current advancing angle under the full load ($I_{A1} = 118$ Apk) are shown in Figure 8. It can be seen that the maximum average torques are obtained when current advancing angle = 53° in the IPM machine, and 62° in the AIPM machine.

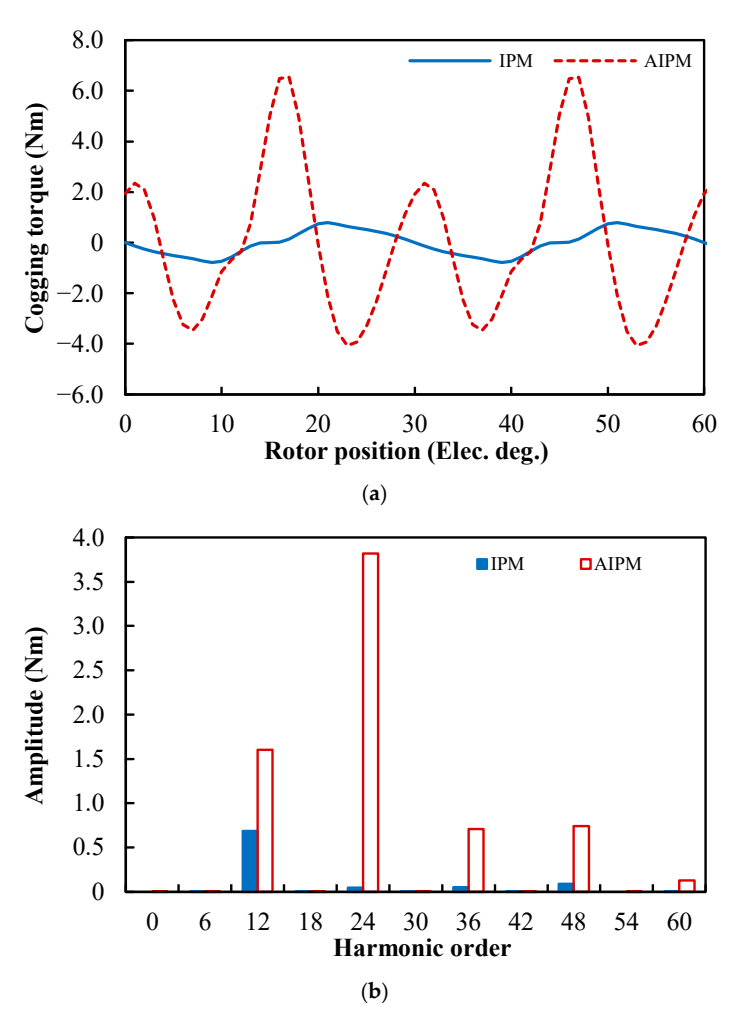


Figure 7. Cogging torques of DTP PMSMs with different rotors. (a) Waveforms. (b) Spectra.

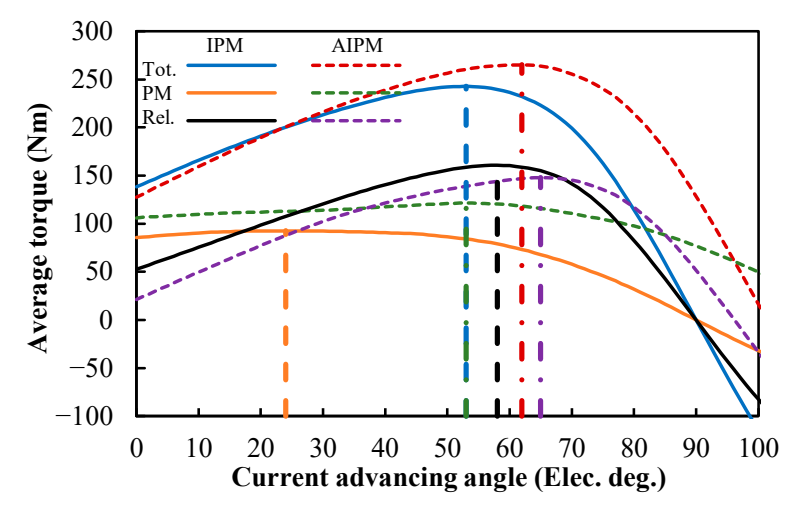


Figure 8. Torque component current advancing angle characteristics of DTP PMSMs with IPM and AIPM rotors ($I_{A1} = 118 \text{ Apk}$).

Energies **2025**, 18, 5477 9 of 28

As mentioned before, in IPM and AIPM machines, the variations in the PM and reluctance torque components with current advancing angle are quite different. With the help of the frozen permeability method [35–37], the PM and reluctance torque components can be separated from the total average torque. The variations in the PM and reluctance torque components with current advancing angle are also presented in Figure 8. It can be found that the optimal current advancing angles for the maximum PM torque component are 24° in the IPM machine, and 53° in the AIPM machine. To achieve the maximum reluctance torque component, the optimal current advancing angles are 58° and 65°, respectively, in IPM and AIPM machines. The current advancing angles to achieve the maximum total, PM, and reluctance torques in the IPM machine were marked with dash lines in the figure. Similarly, the current advancing angles to obtain the maximum total, PM, and reluctance torques in the AIPM machine were marked with dot-dash lines in Figure 20. The optimal current advancing angles for different torque components are summarized in Table 2. In the IPM machine, the difference between the optimal current advancing angles for the maximum PM and reluctance torque components is 34°, but in the AIPM machine, the difference is only 12°. It can be concluded that compared with the IPM rotor, the PM and reluctance torque components in the DTP PMSMs can be better utilized by using the AIPM rotor.

Table 2. Maximum torque components and optimal current advancing angles of DTP PMSMs with IPM and AIPM rotors ($I_{A1} = 236$ APK).

Torque	Maximum V	Value (Nm)	Optimal Current	Advancing Angle (°)
Component	IPM	AIPM	IPM	AIPM
Tot. torque	242.77	265.22	53	62
PM torque	92.73	121.40	24	53
Rel. torque	160.70	147.87	58	65

In Figure 8 and Table 2, it can be seen that, under the full load ($I_{A1} = 118$ Apk), to achieve the maximum average torque, the optimal current advancing angles are 53° and 62°, respectively, in IPM and AIPM machines. With the optimal current advancing angles, the waveforms and spectra of the instantaneous torque in the DTP PMSMs with IPM and AIPM rotors are shown in Figure 9. The average torque and torque ripple characteristics of the PMSMs under the full load are summarized in Table 3. It can be seen that compared with the DTP IPM machine, the DTP AIPM machine can increase the average torque by 9.25% and reduce the torque ripple by 47.62% under the full load.

Table 3. Torque characteristics of DTP IPM and AIPM machines ($I_{A1} = 118$ APK).

	IPM	AIPM	Change
Average torque (Nm)	242.77	265.22	+9.25%
Peak-peak value (Nm)	24.28	13.89	-42.78%
Torque ripple (%)	10.00	5.24	-47.62%

The prototype DTP PMSMs in this paper are modified from the STP PMSMs in [30], by changing the winding configurations and optimizing the rotor design. With the STP windings, the torque characteristics of the STP PMSMs under the full load are provided in Table 4. The results for DTP and STP PMSMs can be compared. Under the full load, the STP AIPM machine can increase the average torque by 8.35% and reduce the torque ripple by 34.08% compared with the STP IPM machine. Hence, by employing the AIPM rotor, DTP PMSM can achieve greater improvements in the average torque and reductions in torque ripple than those in STP PMSM, which may be due to the more severe magnetic saturation in the DTP PMSM.

Energies **2025**, 18, 5477 10 of 28

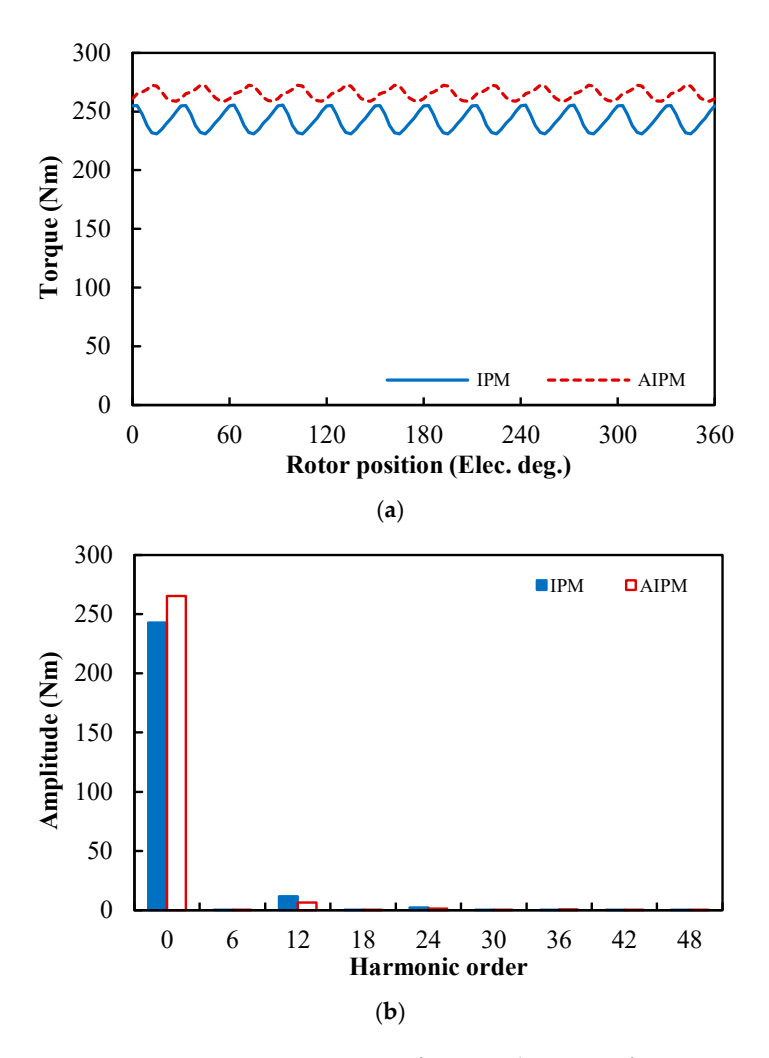


Figure 9. Instantaneous torque waveforms and spectra of DTP PMSMs with IPM and AIPM rotors ($I_{A1} = 118 \text{ Apk}$). (a) Waveforms. (b) Spectra.

Table 4. Torque characteristics of STP IPM and AIPM machines ($I_{A1} = 236$ APK).

	IPM	AIPM	Change
Average torque (Nm)	236.50	256.26	+8.35%
Peak-peak value (Nm)	35.99	25.71	-28.58%
Torque ripple (%)	15.22	10.03	-34.08%

Under other load conditions, the optimal current advancing angles can also be obtained based on the maximum torque per amplitude (MTPA) control strategy. In the DTP IPM and AIPM machines, assuming I_{A1} varies from 25 Apk to 250 Apk to cover the load conditions from light-load to over-load, the variations in average torques and torque ripples with phase current amplitude are shown in Figure 10a,b, respectively. It can be seen that the average torque of the DTP PMSM can always be improved significantly by using the AIPM rotor, and the average torque improvements are presented in Figure 10c. In addition, when the phase current \geq 75 Apk, not only can the average torque be improved, but the torque ripple can also be reduced using the AIPM rotor. Hence, the AIPM rotor can greatly improve the torque performance of the DTP PMSM.

Energies 2025, 18, 5477 11 of 28

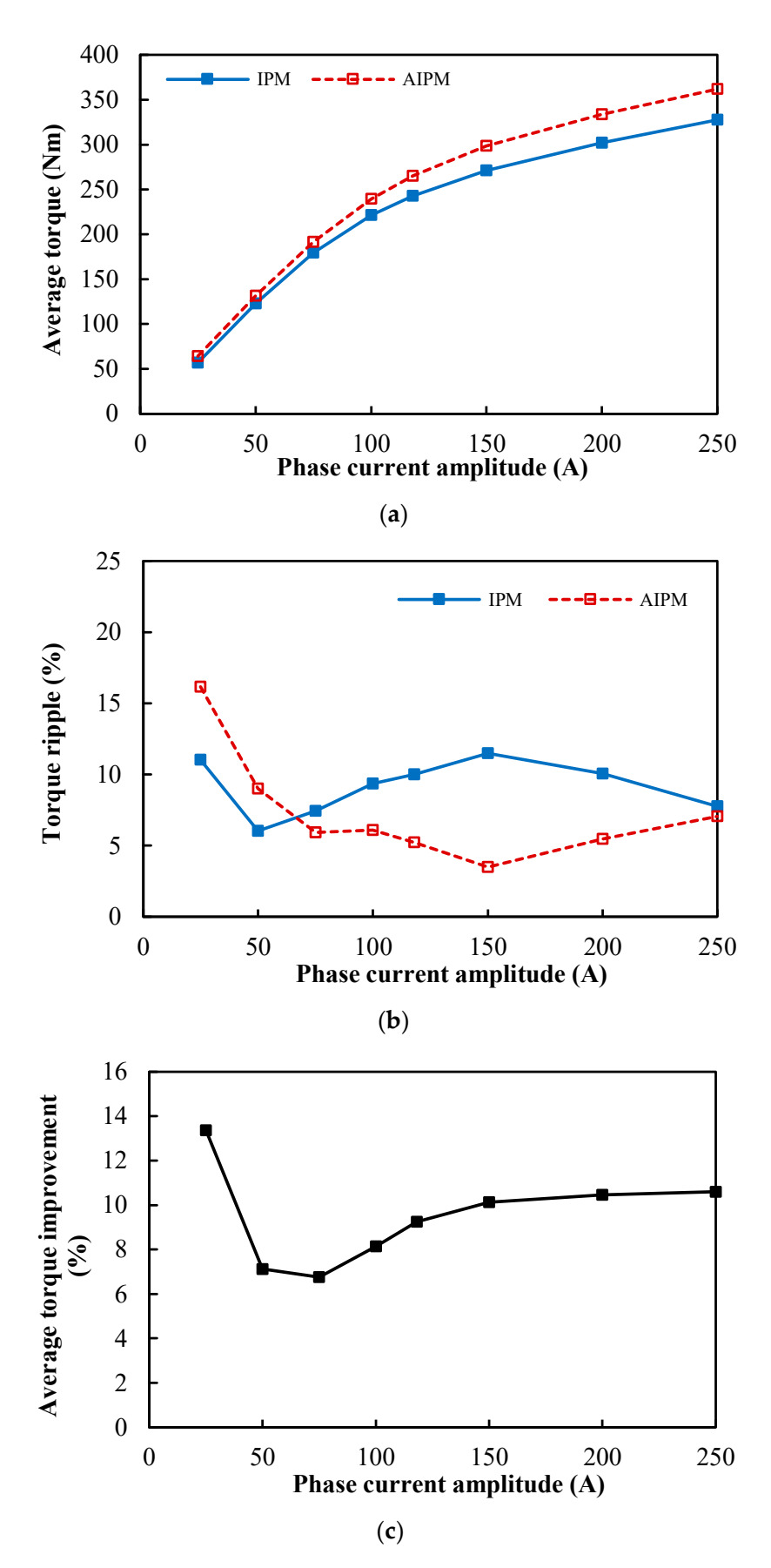


Figure 10. Variations in torque characteristics with phase current amplitude in DTP PMSMs with IPM and AIPM rotors. (a) Average torque. (b) Torque ripple. (c) Average torque improvement.

Energies 2025, 18, 5477 12 of 28

3.3. Loss and Efficiency

In this paper, the losses and efficiencies of the DTP PMSMs with IPM and AIPM rotors are obtained by using the method in [38]. The copper loss is calculated, using Joule's law, as follows:

$$P_{Cu} = 3R_0 I_a^2 (1)$$

where R_0 is the phase resistance of the DTP windings, and I_a is the phase current amplitude. The calculation of iron losses consists of hysteresis and eddy current iron losses, which are calculated using the following:

$$P_{Fe} = P_{Hyst-base} \frac{f}{f_{base}} + P_{Eddy-base} \left(\frac{f}{f_{base}}\right)^2 \tag{2}$$

where $P_{Hyst-base}$ and $P_{Eddy-base}$ are the hysteresis and eddy current iron losses at the base speed, i.e., 3000 rpm in this study, and f and f_{base} are the frequencies of the operating condition and the base speed, respectively.

PM eddy current losses are obtained from FE simulations directly, and mechanical losses are estimated by [39].

$$P_{Me} = 0.26f + 0.00103f^2 (3)$$

Overall, the loss characteristics of the DTP PMSMs with IPM and AIPM rotors under the full load ($I_{A1} = 118$ Apk, speed = 3000 rpm) are summarized and compared in Table 5.

	IPM	AIPM
Average output torque (Nm)	242.76	265.21
Output power (kW)	76.27	83.32
Copper loss (W)	7283.49	7283.49
Stator iron loss (W)	338.27	325.81
Rotor iron loss (W)	28.62	27.49
Total iron loss (W)	366.89	353.30
PM eddy current loss (W)	63.28	86.05
Mechanical loss (W)	93.20	93.20
Total loss (kW)	7.81	7.82
Efficiency (%)	90.71	91.42

Table 5. Loss and efficiency of DTP PMSMs with IPM and AIPM rotors ($I_{A1} = 118$ APK at 3000 RPM).

It can be found that the total losses in IPM and AIPM machines are 7.81 kW and 7.82 kW, respectively. In other words, the asymmetric IPM rotor could only slightly affect total losses. It can be further inferred that the temperature performance of the DTP PMSMs with IPM and AIPM rotors will not show evident differences, as presented in the STP counterparts [30].

It can be seen that copper loss is the most dominant loss in both the IPM and AIPM machines. Since the IPM and AIPM machines share the same stator and armature windings, the copper losses of the two DTP PMSMs are identical. Due to similar iron loss and higher PM eddy current loss, the total loss in the AIPM machine is slightly higher than that in its IPM counterpart. However, considering that the output torque and output power of the AIPM machine are obviously larger than those of the IPM counterpart, the AIPM machine still has higher overall efficiency than the IPM counterpart under this condition.

To analyze the loss and efficiency characteristics of the DTP PMSMs with IPM and AIPM rotors at other speeds, the torque and power–speed curves of the two DTP PMSMs are calculated under the constraints.

Energies 2025, 18, 5477 13 of 28

To analyze the loss and efficiency characteristics of the DTP PMSMs with IPM and AIPM rotors at other speeds, the torque and power–speed curves of the two DTP PMSMs are calculated under the constraints (DC link voltage \leq 650 Vdc and phase current \leq 118 Apk), as shown in Figure 11. Similarly, the variations in the maximum d- and q-axis currents (I_d and I_q), and phase currents (I_a) with speed are shown in Figure 12. It can be clearly seen that the AIPM machine can produce higher torque than the IPM counterpart, not only in constant torque region (low speed), but also in constant power region (high speed).

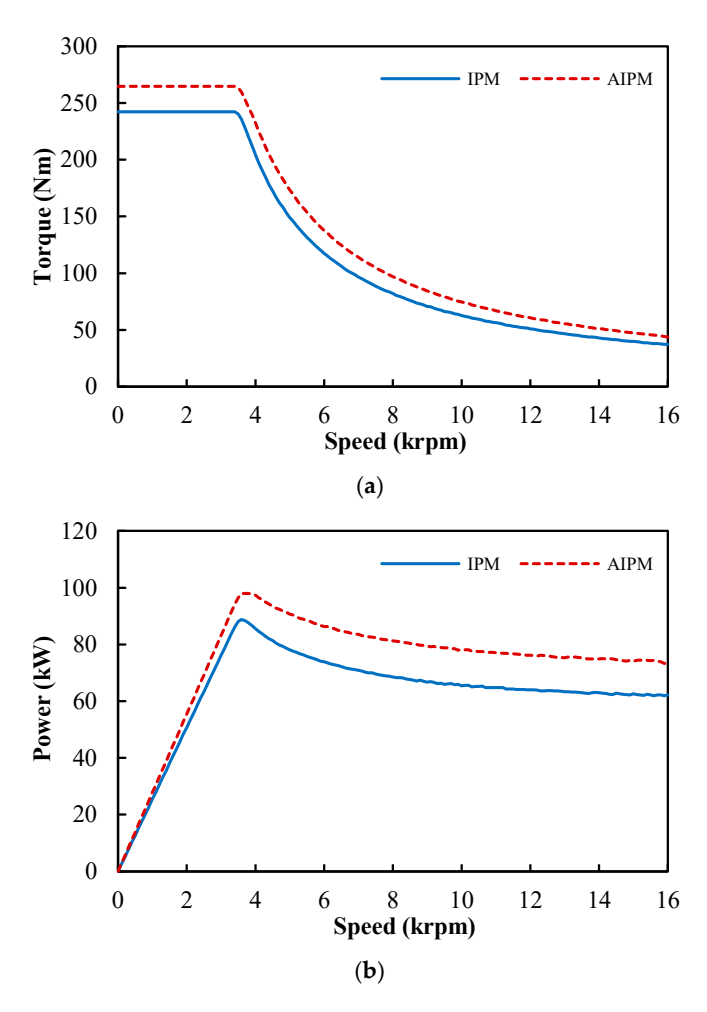


Figure 11. Torque and power–speed curves of DTP PMSMs with IPM and AIPM rotors. (a) Torque–speed curves. (b) Power–speed curves.

Based on (1), (2), and Figures 11 and 12, the copper loss and iron loss maps of the DTP PMSMs with IPM and AIPM rotors are calculated, as shown in Figures 13 and 14, respectively. The mechanical losses of the DTP IPM and AIPM machines are calculated by using (3), as shown in Figure 15.

Considering that the PM eddy current loss under other speeds cannot be estimated directly from the base speed, and that the PM eddy current loss is very small in total loss, as indicated in Table 5, the disregard of PM eddy current loss in the calculation of resultant efficiency is still acceptable. Thus, when ignoring PM eddy current loss, the total loss maps of the DTP IPM and AIPM machines can be obtained from Figures 13–15, as shown in Figure 16. The total loss difference between the AIPM and IPM machines is given in Figure 16c. In Figure 16c, the operating conditions can be classified into three conditions: low-speed and low-torque, low-speed and high-torque, and high-speed conditions. It can be observed that at high speed, iron loss is the dominant loss and the AIPM machine has higher total loss, while at low speed and high torque, copper loss is the dominant loss and

Energies 2025, 18, 5477 14 of 28

the IPM machine has higher total loss. At low speed and low torque, the AIPM and IPM machines show similar total losses.

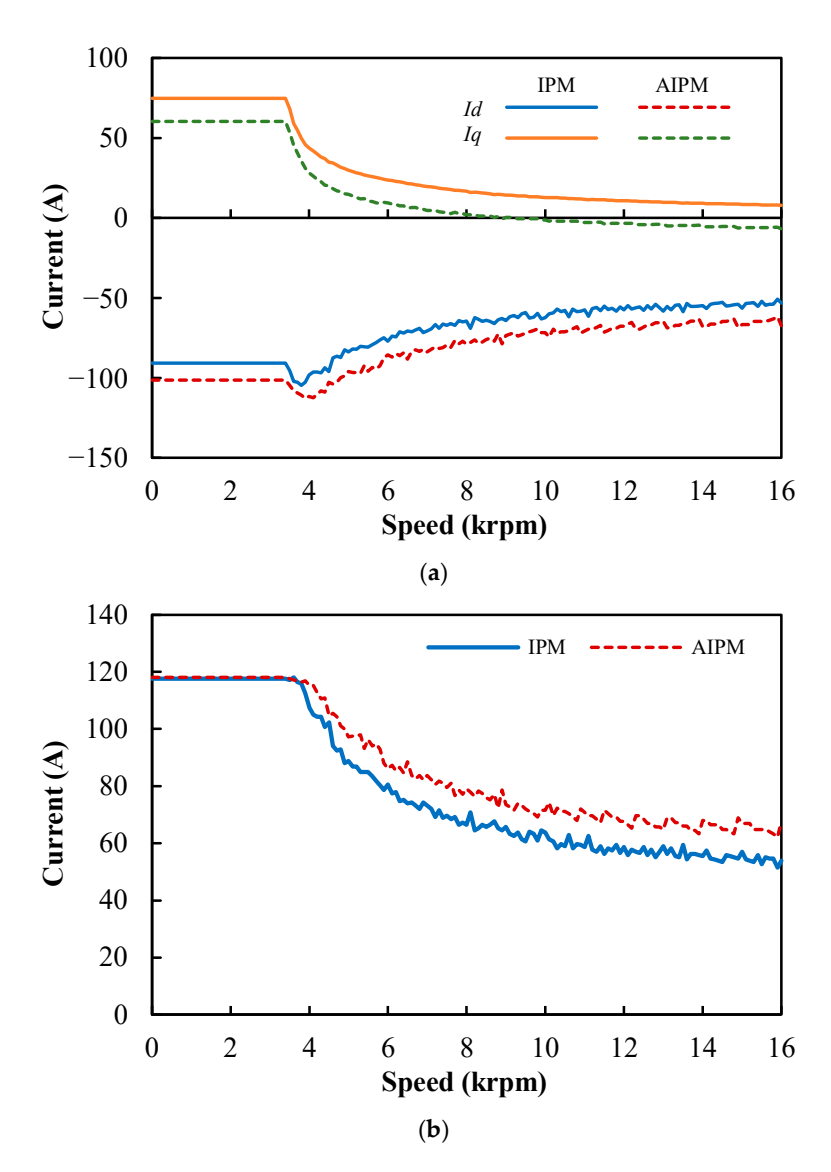


Figure 12. Current-speed curves of DTP PMSMs with IPM and AIPM rotors. (a) I_d - and I_q -speed curves. (b) I_a -speed curves.

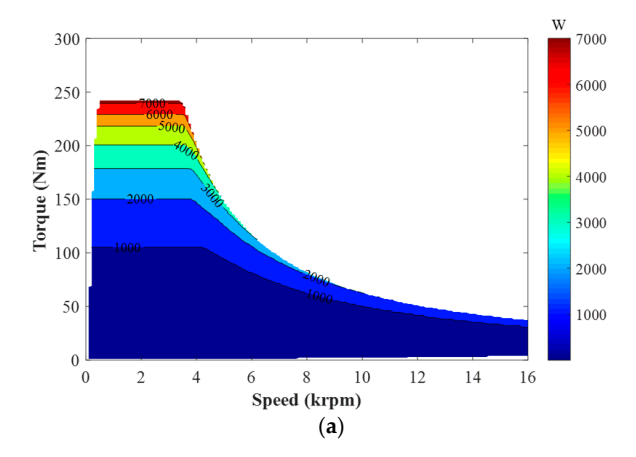


Figure 13. Cont.

Energies 2025, 18, 5477 15 of 28

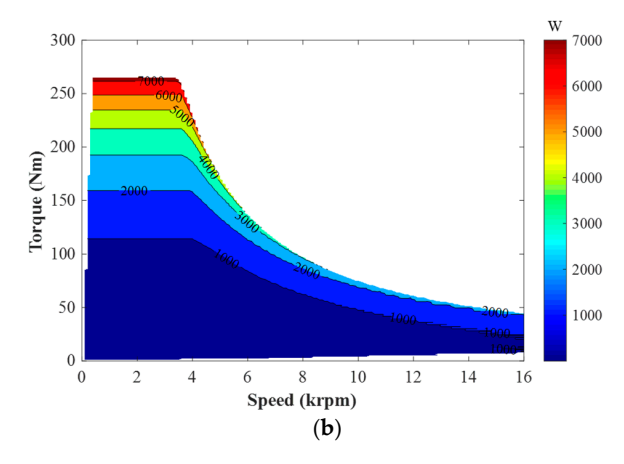


Figure 13. Copper loss maps of DTP PMSMs with IPM and AIPM rotors. (a) IPM. (b) AIPM.

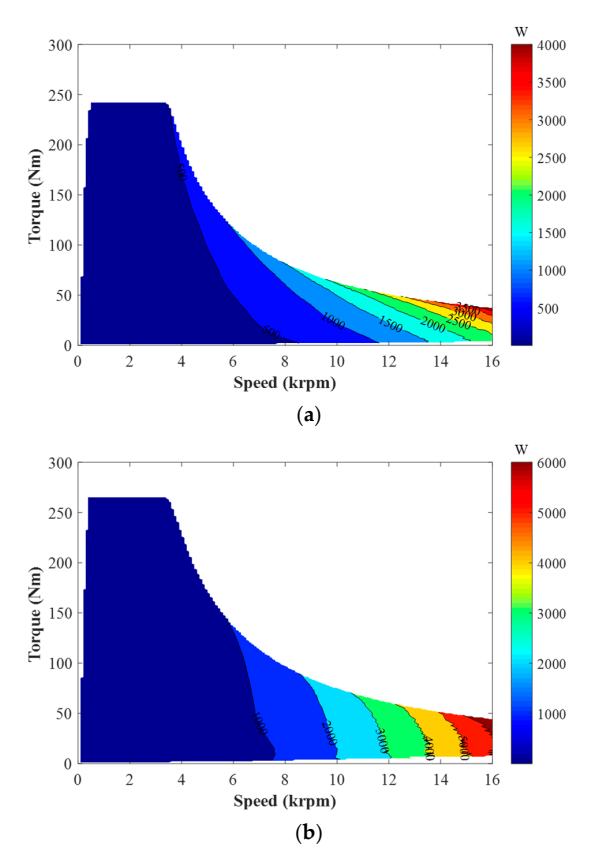


Figure 14. Iron loss maps of DTP PMSMs with IPM and AIPM rotors. (a) IPM. (b) AIPM.

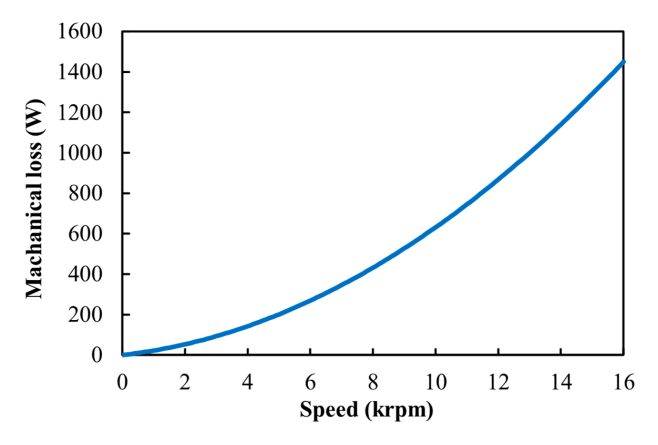


Figure 15. Mechanical loss of DTP PMSMs with IPM and AIPM rotors.

Energies **2025**, 18, 5477

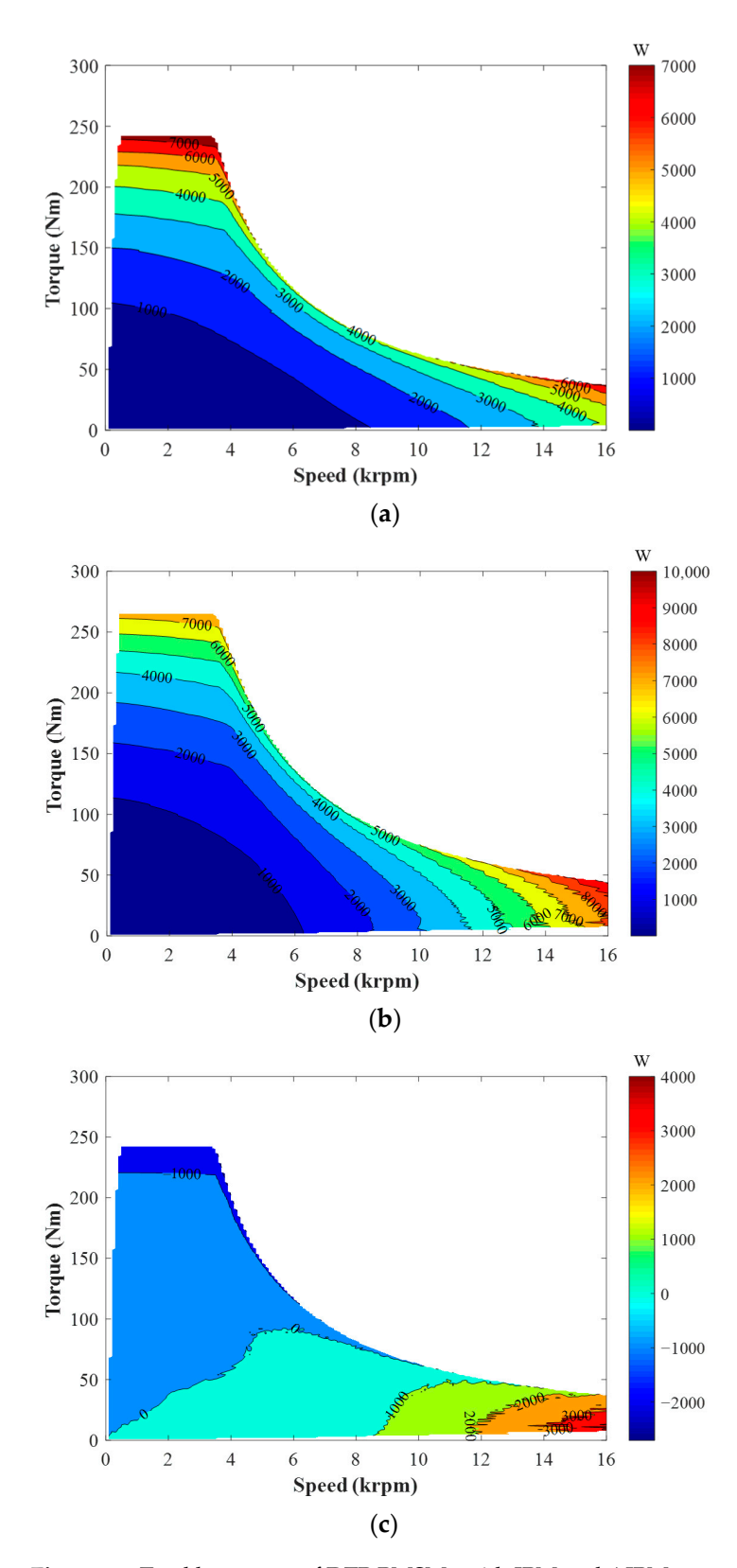


Figure 16. Total loss maps of DTP PMSMs with IPM and AIPM rotors. (a) IPM. (b) AIPM. (c) Total loss difference (AIPM—IPM).

In Figure 14, it can be observed that the iron loss in the AIPM machine is higher than that in the IPM counterpart at high speed, and at low speed and low torque. However, as shown in Table 5, the iron loss of the AIPM machine is slightly lower than that of the IPM counterpart at the full load (low speed and high torque). Considering that the phase

Energies **2025**, 18, 5477 17 of 28

currents under different operating conditions are different, it is necessary to further analyze the effects of electric loading on iron losses in the DTP AIPM and IPM machines.

Assuming the phase currents vary from 0 to 250 Apk, the iron losses of the DTP PMSMs with the IPM and AIPM rotors at 3000 rpm are compared in Figure 17. It can be observed that the iron loss in the DTP AIPM machine is higher than that in the IPM counterpart at low currents (\leq 50 Apk), but lower than that in the IPM counterpart at high loads (≥75 Apk). This phenomenon can be explained by the different air-gap MMF harmonic contents in the AIPM and IPM machines. When electric loading is low, the air-gap MMF is mainly produced by rotor PMs. Under open-circuit conditions, the air-gap flux densities of the DTP AIPM and IPM machines are shown in Figure 5. In Figure 5b, it can be seen that the AIPM machine has a higher fundamental component (0.77 T in the IPM machine, and 0.92 T in the AIPM machine) and more abundant harmonic contents (THD = 42.66% in the IPM machine, 68.42% in the AIPM machine). Hence, the iron loss of the DTP AIPM machine is significantly higher than that in the DTP IPM machine under lowload conditions. However, with the increase in phase currents, the air-gap flux densities of the DTP AIPM and IPM machines are mainly affected by armature windings, and less affected by rotor PMs. Under the full-load conditions ($I_{A1} = 118$ Apk), the air-gap flux densities of the DTP AIPM and IPM machines are compared in Figure 18.

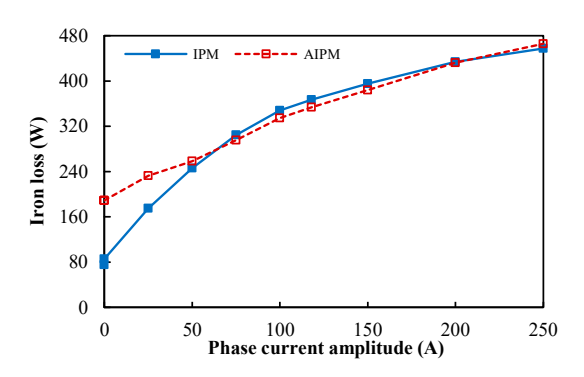


Figure 17. Variations in iron losses with phase current amplitude in DTP PMSMs with IPM and AIPM rotors.

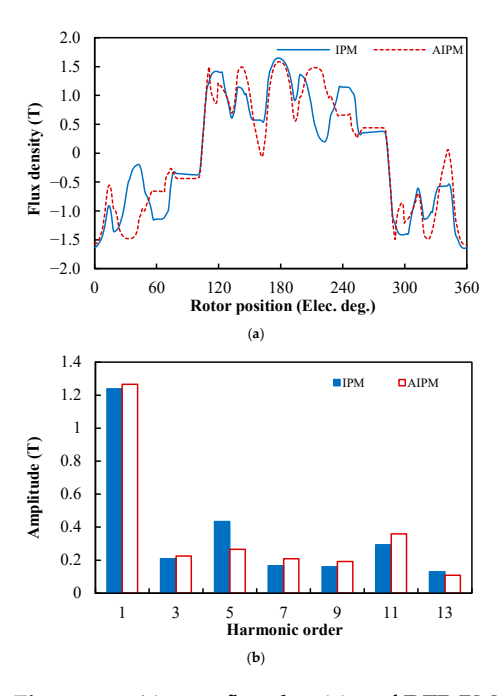


Figure 18. Air-gap flux densities of DTP PMSMs with different rotors under full-load conditions ($I_{A1} = 118 \text{ Apk}$). (a) Waveforms. (b) Spectra.

Energies 2025, 18, 5477 18 of 28

It can be seen that the air-gap flux densities of the DTP IPM and AIPM machines are close to each other under this condition. In addition, due to the different rotor layouts, the harmonic contents in the AIPM machine are even lower than those in the IPM counterpart under this condition (THD = 41.57% in the IPM machine, 38.44% in the AIPM machine). As a result, compared with the DTP IPM machine, the DTP AIPM machine shows higher iron loss when electric loading is low (under low-speed and low-torque, and high-speed conditions) and lower iron loss when electric loading is high (at low speed and high torque).

Based on Figure 16, the efficiency maps of the DTP PMSMs with IPM and AIPM rotors are calculated, as shown in Figure 19a,b, respectively. The efficiency difference between the AIPM and IPM machines is presented in Figure 19c.

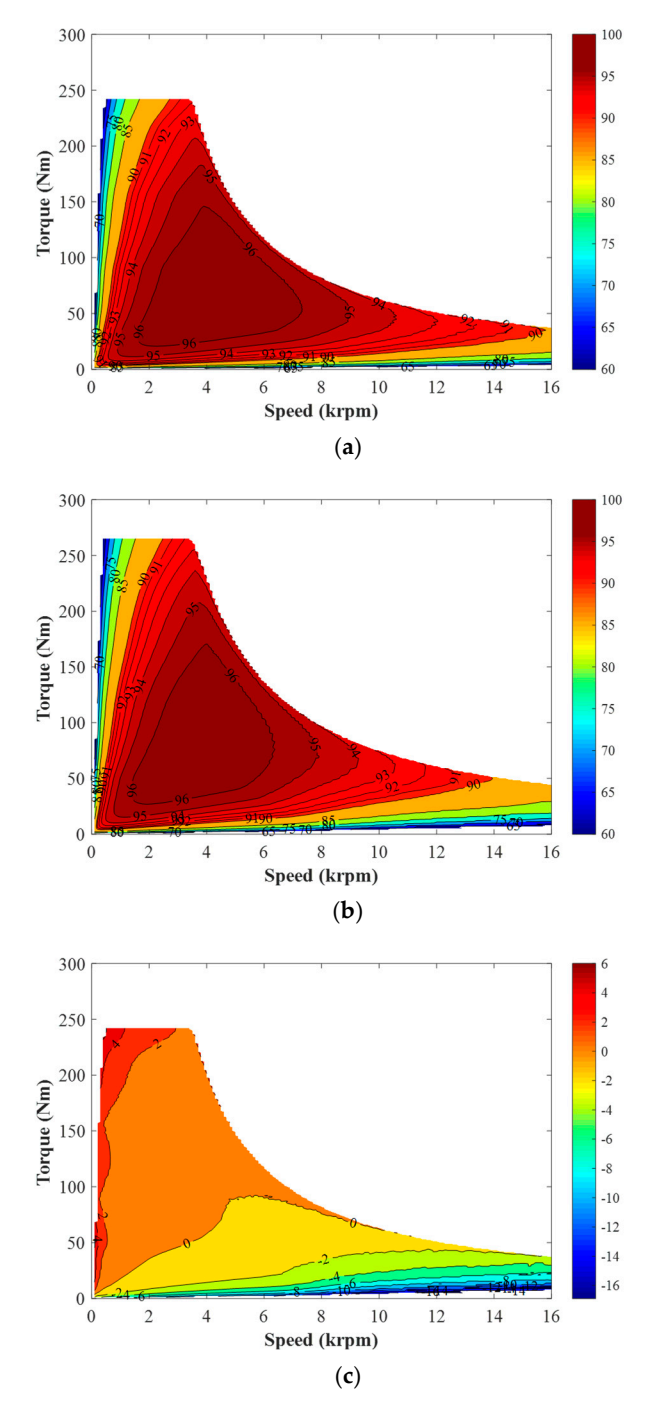


Figure 19. Efficiency maps of DTP PMSMs with IPM and AIPM rotors. (a) IPM. (b) AIPM. (c) Efficiency difference (AIPM—IPM).

Energies **2025**, 18, 5477 19 of 28

It can be found that the DTP AIPM and IPM machines show higher efficiencies under different operating conditions. Due to the more abundant PM MMF harmonics in the DTP AIPM machine, the DTP AIPM machine shows a higher iron loss and lower efficiency than the IPM counterpart at high speed. However, when electric loading is higher, the iron losses due to armature reaction field become more significant and hence the iron losses in IPM and AIPM machines become more similar to each other. Thus, the investigated DTP AIPM topology exhibits higher efficiency than the IPM counterpart at high-torque and high-load conditions, due to the optimization goal only focusing on higher torque density [39].

4. Torque Characteristics Under Three-Phase OC Conditions

Since the two three-phase winding sets in DTP PMSMs are connected independently, any fault in one three-phase winding set will not result in the failure of the total torque output and DTP PMSMs can still operate with only one three-phase winding set. The torque characteristics of the DTP PMSMs with IPM and AIPM rotors under single three-phase OCs are compared.

As mentioned before, in the analyzed IPM and AIPM machines, the phase current amplitude is 118 A under a healthy full load. When the phase current amplitude is 118 A under single three-phase OC conditions (I_{A1} = 118 Apk, IA2 = 0), the variations in the total torque, PM torque, and reluctance torque with current advancing angle are shown in Figure 20. For the IPM machine, the current advancing angles to achieve the maximum total, PM, and reluctance torques were marked with dash lines in the figure. Similarly, the current advancing angles to obtain the maximum total, PM, and reluctance torques in the AIPM machine were marked with dot-dash lines in Figure 20. The optimal current advancing angles under this condition are summarized in Table 5. The difference between the optimal current advancing angles for the maximum PM and the reluctance torque components is 25° for the IPM machine and 19° for the AIPM machine. Hence, under single three-phase OC conditions, the MFS effect can still be observed, and thus, the AIPM rotor can still improve the average torque.

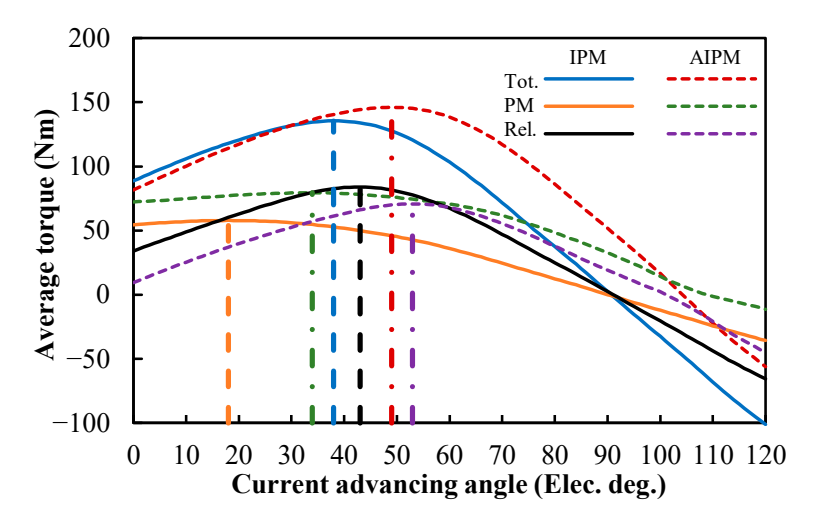


Figure 20. Torque component current advancing angle characteristics of DTP PMSMs with IPM and AIPM rotors under single three-phase OC conditions (I_{A1} = 118 Apk).

In Table 6, under single three-phase OC conditions, when I_{A1} = 118 Apk, the maximum average torques in the IPM and AIPM machines are obtained with current advancing angle = 38° and 49°, respectively. The waveforms and spectra of the instantaneous torque in the DTP PMSMs with IPM and AIPM rotors under this condition are shown in Figure 21, and the torque characteristics are summarized in Table 7. It can be seen that the average

Energies 2025, 18, 5477 20 of 28

torque can still be improved significantly by the AIPM rotor, but the torque ripple is increased slightly by the AIPM rotor.

Table 6. Maximum torque components and optimal current advancing angles of DTP PMSMs with IPM and AIPM rotors ($I_{A1} = 118$ APK).

Torque	Maximum Value (Nm)		Optimal Current	Advancing Angle (°)
Component	IPM	AIPM	IPM	AIPM
Tot. torque	135.53	146.09	38	49
PM torque	57.88	79.45	18	34
Rel. torque	83.99	70.82	43	53

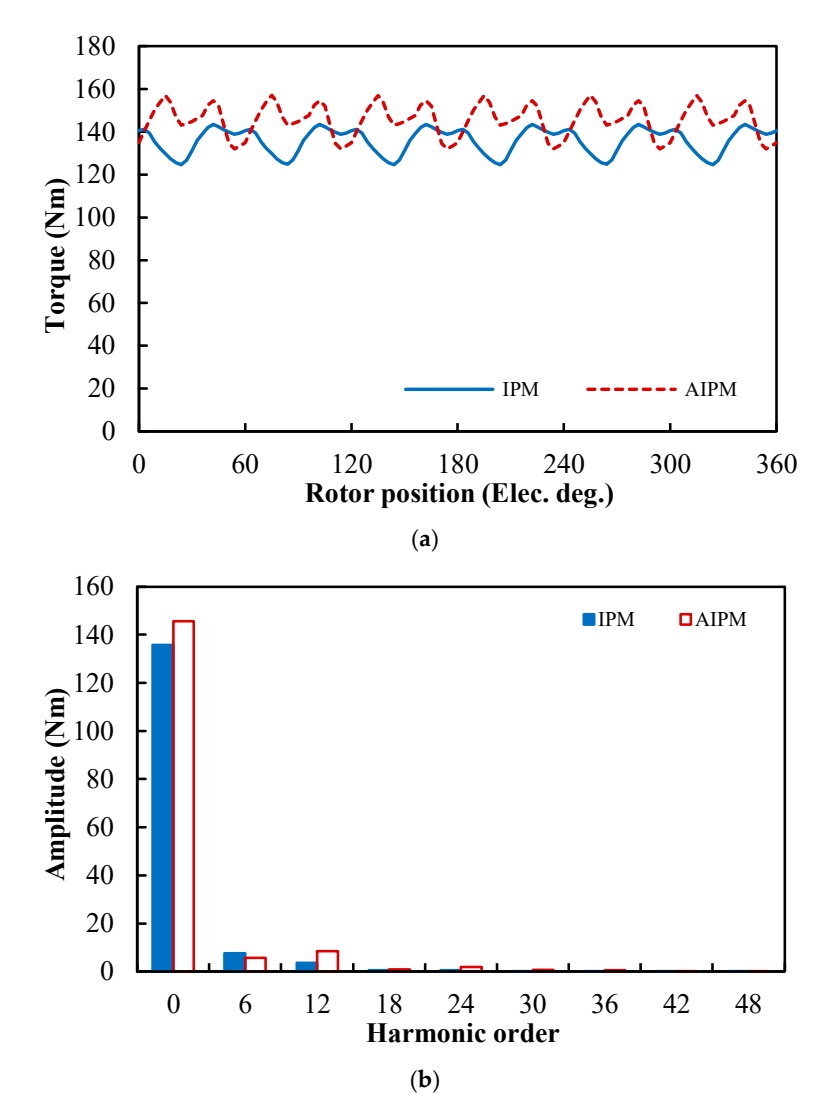


Figure 21. Instantaneous torque waveforms and spectra of DTP PMSMs with IPM and AIPM rotors under three-phase OC conditions ($I_{A1} = 118$ Apk). (a) Waveforms. (b) Spectra.

Table 7. Torque characteristics of DTP IPM and AIPM machines under three-phase OC conditions ($I_{A1} = 118 \text{ APK}$).

	IPM	AIPM	Change
Average torque (Nm)	135.80	145.54	+7.17%
Peak-peak value (Nm)	18.79	25.09	+33.54%
Torque ripple (%)	13.83	17.24	

Energies 2025, 18, 5477 21 of 28

Similarly to the analyses under healthy conditions, when one three-phase winding set is open-circuited and I_{A1} varies from 25 Apk to 250 Apk, the variations in average torques and torque ripples with phase current amplitude are shown in Figure 22a,b, respectively. It can be seen that the average torque can still be improved by the AIPM rotor, and the torque improvements are summarized in Figure 22c. However, the torque ripple can only be reduced when the phase current \geq 150 Apk. Overall, the AIPM rotor can still achieve significant torque improvement in the DTP PMSM under the single three-phase OC condition.

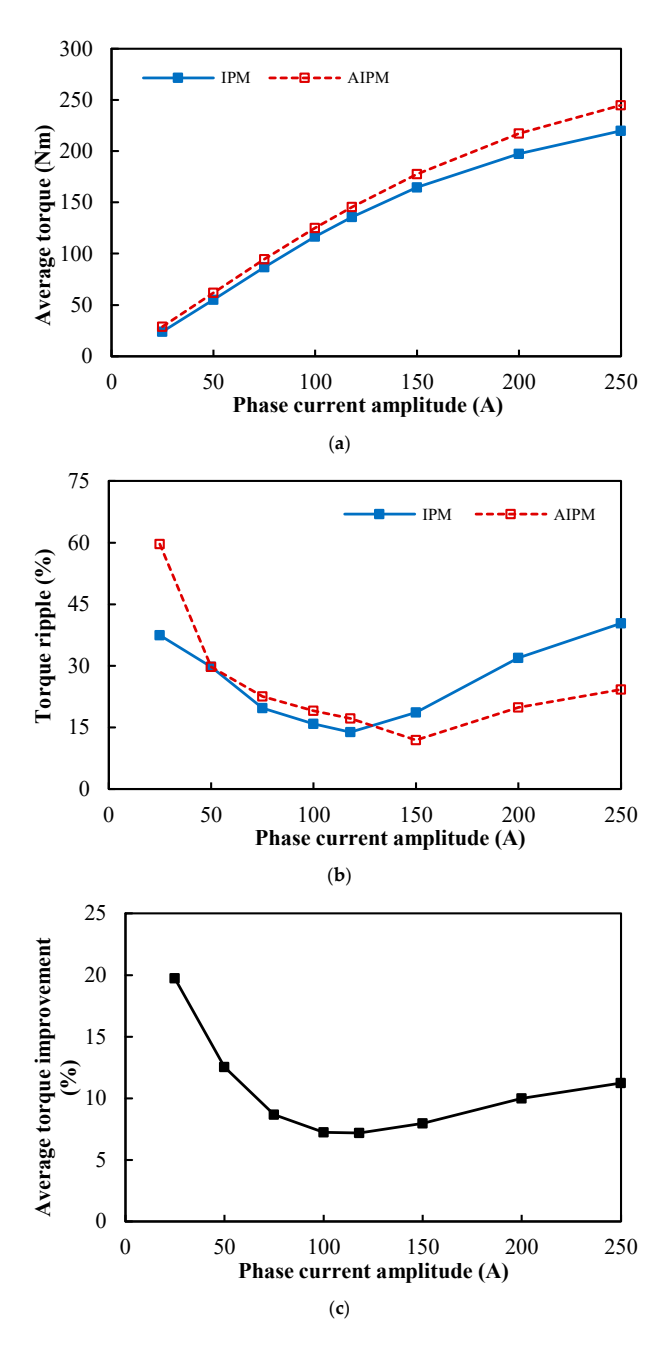


Figure 22. Variations in torque characteristics with phase current amplitude in DTP PMSMs with IPM and AIPM rotors under three-phase OC conditions. (a) Average torque. (b) Torque ripple. (c) Average torque improvement.

5. Experimental Verification

Considering the difficulties in manufacturing and testing a large prototype which shares the same size as the Toyota Prius 2010 machine, small-scale 24-slot/4-pole pro-

Energies 2025, 18, 5477 22 of 28

totypes are fabricated and tested to verify the FE analyses presented in this paper. The prototype DTP PMSMs are modified from the STP PMSMs in [39] by changing the winding configurations.

Some key design specifications of the prototype are given in Table 8. The pictures of the DTP AIPM prototype are given in Figure 23, and the test rig is shown in Figure 24.

Table 8. Main design specifications of the 24-slot/4-pole prototype DTP AIPM machine.

Parameters	Values			
Sta	Stator			
Stator OD, mm	100.0			
Stator ID, mm	50.0			
Stack length, mm	50.0			
Slot depth, mm	18.5			
Slot opening, mm	2.0			
Stator material	Silicon steel sheet (B35A250)			
AIPM	AIPM Rotor			
Rotor OD, mm	48.0			
Rotor ID, mm	14.0			
Stack length, mm	50.0			
Rotor material	Silicon steel sheet (B35A250)			
Large PM length, mm	15.5			
Large PM thickness, mm	3.5			
Small PM length, mm	5.5			
Small PM thickness, mm	2.0			
PM material	NdFeB (N38)			
PM remanence, T	1.23			
PM relative permeability	1.04			

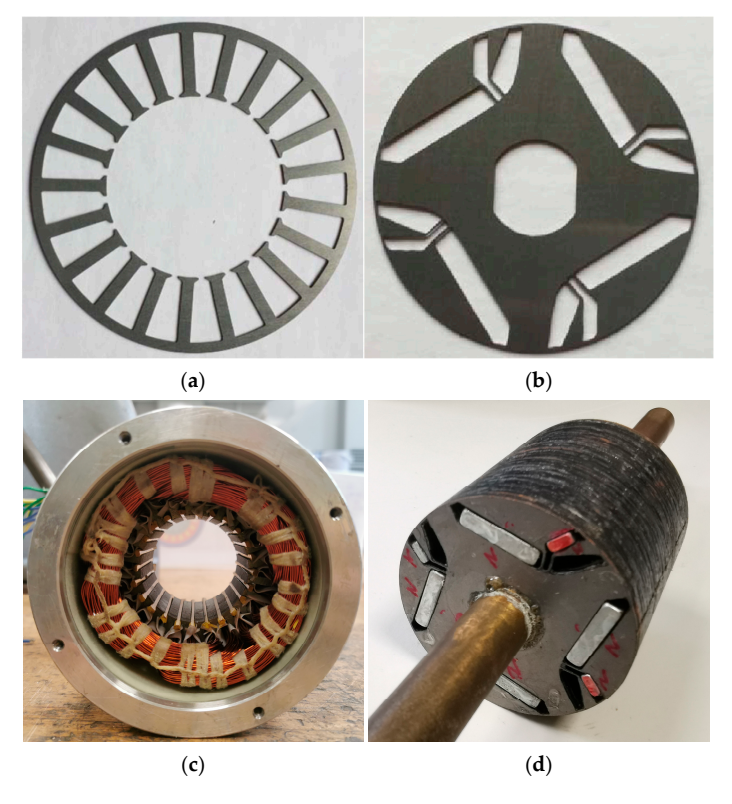


Figure 23. Pictures of the prototype DTP PMSM with AIPM rotor. (a) Stator lamination. (b) Rotor lamination. (c) Stator. (d) Rotor.

Energies 2025, 18, 5477 23 of 28



Figure 24. Picture of test rig.

The FE predicted and measured waveforms and spectra of phase back EMF and cogging torque are compared in Figures 25 and 26. The cogging toque is measured by using the method proposed in [40]. In the prototype machine, the phase back EMFs exhibit significant harmonics due to the asymmetric rotor layout. In Figure 25a, an asymmetric half waveform can be observed due to the small magnet between the large magnet and the flux barrier. It can also be found from Figure 25b that the measured fundamental and harmonic amplitudes are lower than the FE predicted results, which could be due to the neglect of end effects in 2D FE calculations. Although the AIPM rotor is not symmetrical from the view of one rotor pole, the whole rotor is still symmetrical as the four rotor poles share the same cyclic layout, and thus, there is no even harmonic in resultant phase back EMFs.

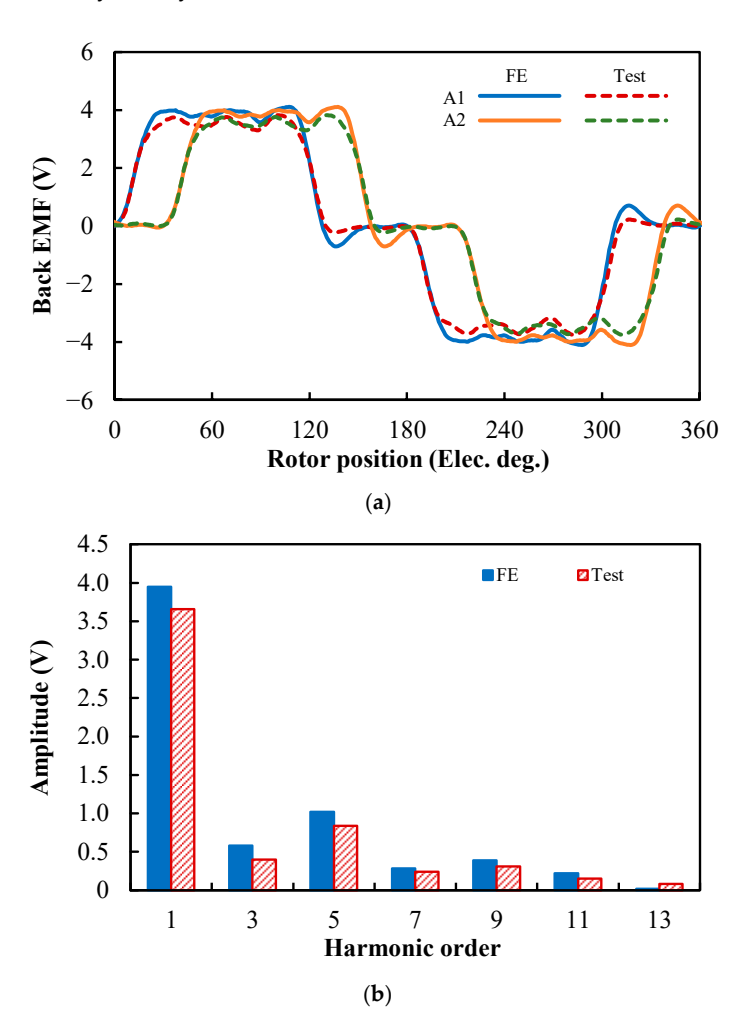


Figure 25. Phase back EMF comparison between FE predicted and measured results at 200 rpm. (a) Waveforms. (b) Spectra.

Energies 2025, 18, 5477 24 of 28

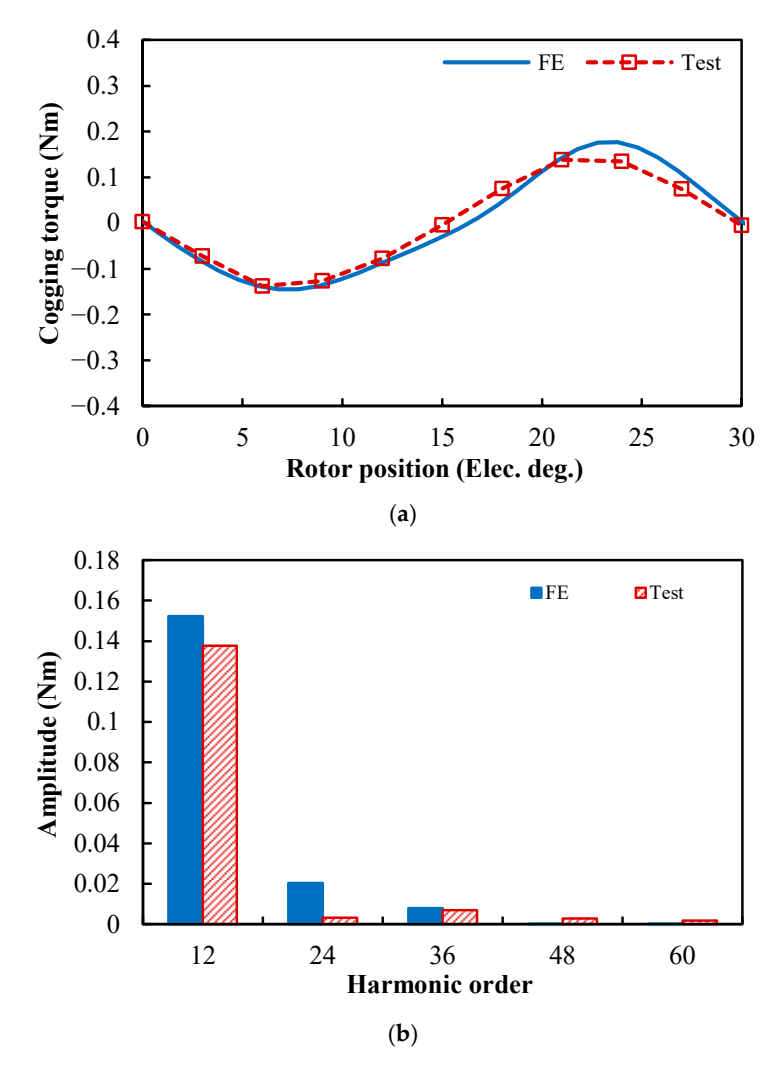


Figure 26. Cogging torque comparison between FE predicted and measured results. (a) Waveforms. (b) Spectra.

Due to the same slot/pole ratio, the fundamental order of cogging torque is 12 in electric for the 24-slot/4-pole prototype, which is identical to that in the 48-slot/8-pole PMSMs. The measured cogging torque validates the order number of the FE predicted results, but the measured cogging torque amplitude is smaller than simulations.

To validate the FE analyses under on-load conditions, it is preferred to measure the torque performances of the prototype at a specific rotational speed. However, considering the difficulties in setting up the drive configurations for the DTP prototype, a simpler method was utilized in the validation. The two three-phase winding sets of the prototype are supplied by direct currents, and the static torque versus rotor position waveforms are measured under different current values. It should be noticed that due to the 30° phase shift between the two winding sets, the phase currents in the two winding sets are different at the same time, as shown in Figure 27. At the time denoted by the gray dash line in Figure 27, the direct currents in different phases can be assigned as $I_{A1} = I_{dc}$, $I_{B1} = I_{C1} = -0.5I_{dc}$, $I_{A2} = 0.866I_{dc}$, $I_{B2} = 0$, and $I_{C2} = -0866I_{dc}$. Thus, the on-load tests can be realized with simply two DC supplies. The first winding set is supplied by a DC supply with I_{dc} . Phases B1 and C1 windings are connected in parallel first and then connected with Phase A1 winding in series. The second winding set is supplied by another DC supply with $0.866I_{dc}$, which is supplied to series-connected Phases A2 and C2 windings. Phase B2 winding is not supplied with current.

Energies **2025**, 18, 5477 25 of 28

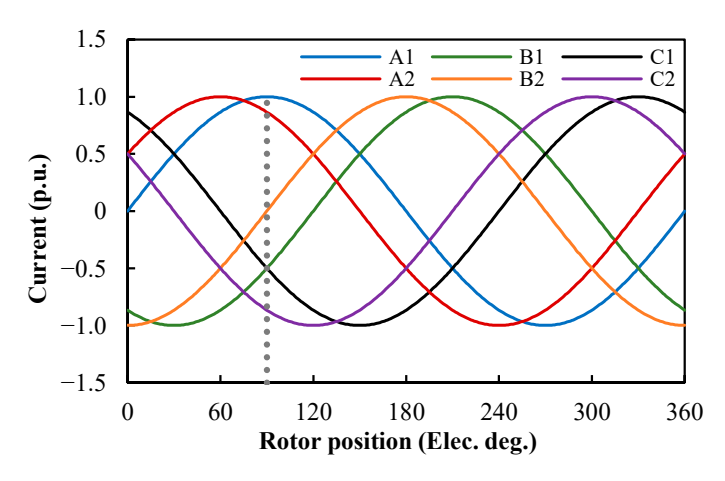


Figure 27. Phase currents for DTP PMSM.

The FE predicted and measured waveforms, as well as their spectra of static torque versus the rotor position characteristics of the prototype machine with different I_{dc} values, are compared in Figure 28. The corresponding variations in the fundamental amplitudes of static torque with I_{dc} are compared in Figure 29. It can be seen that the measured results are lower than the FE predicted results, due to the neglecting of the end-winding effects in 2D FE calculations.

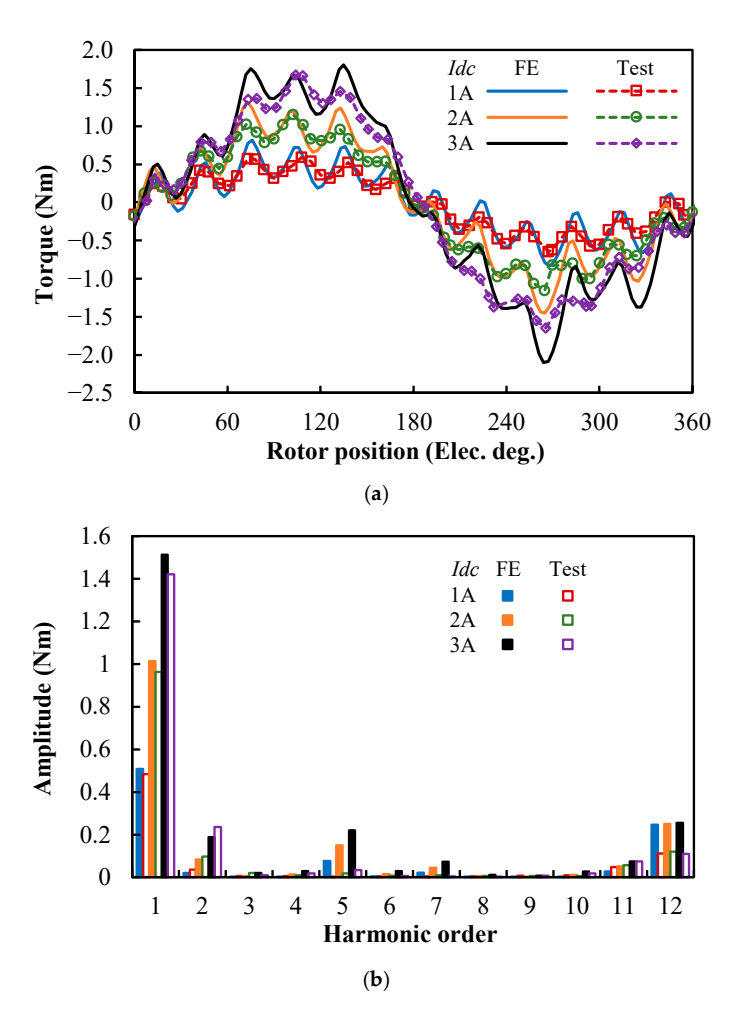


Figure 28. Static torque comparison between FE predicted and measured results with different I_{dc} values. (a) Waveforms. (b) Spectra.

Energies **2025**, 18, 5477 26 of 28

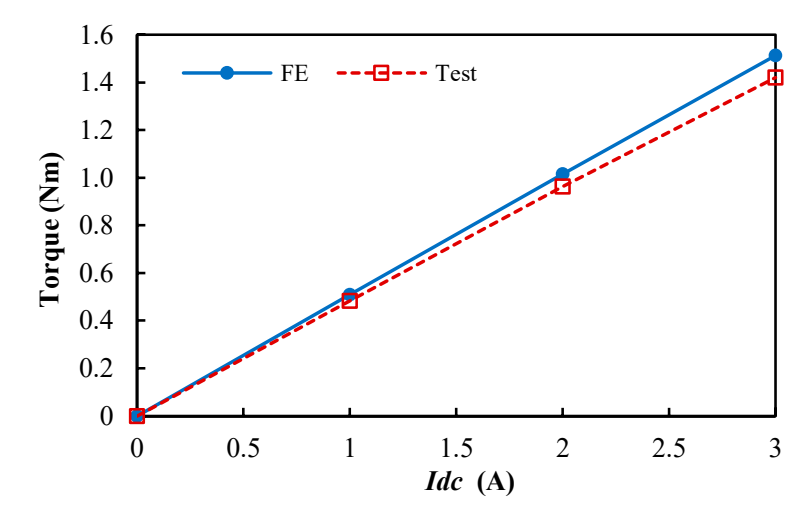


Figure 29. Variations in FE predicted and measured fundamental static torque amplitudes with I_{dc} .

Overall, the agreement between the FE predicted and the tested results under OC and on-load conditions validate the accuracy of the FE analyses and conclusions drawn in this paper.

6. Conclusions

In this paper, the effects of an AIPM rotor topology on the electromagnetic performance of DTP PMSMs are investigated and compared with those obtained with the symmetrical IPM rotor, based on the Toyota Prius 2010 machine configuration. Both healthy and single three-phase OC conditions are considered. It is found that the MFS effect also exists in DTP PMSMs both under healthy and single three-phase OC conditions, and thus, the average torque can be improved significantly by using the AIPM rotor. Furthermore, it is found that in DTP PMSMs, the average torque improvement by the AIPM rotor is higher than that in STP PMSMs.

Overall, the benefits of AIPM rotors in STP PMSMs, such as the higher average torque and lower torque ripple, still exist in DTP PMSMs, and the torque improvement can still be achieved even under single three-phase OC conditions in DTP PMSMs. It also should be noticed that these results were obtained using a specific rotational direction. Due to the special asymmetric rotor topology, the results are not applicable for the other rotational direction. For the PMSMs with AIPM rotors, the torque performances are different under different rotational directions and some further analyses can be found in [26].

The DTP winding configuration and AIPM rotor can both improve average torque in PMSMs. In the benchmark Toyota Prius 2010 machine, it was found that the torque improvement by DTP windings was 2.65%, by the AIPM rotor was 8.35%, and by the "DTP windings + AIPM rotor" was 12.14%. The idea is that "DTP windings + AIPM rotor" can be utilized in the conditions where higher torque capability is required but there is no space for the updating, as the two methods (DTP winding configuration and AIPM rotor) do not change the volume of the original machine. In addition, it is also found that due to the more abundant PM MMF harmonics, the DTP AIPM machine shows higher iron loss and lower efficiency than the symmetrical IPM counterpart when the torque load is low, particularly in the high-speed region, albeit to the torque enhancement across all regions. However, when electric loading is higher, the iron losses due to the armature reaction field become more significant and hence the difference between the iron losses in IPM and AIPM machines becomes smaller. As traction machines in EVs have variable operation conditions, the AIPM rotor design for DTP machines in EV applications should be comprehensively

Energies **2025**, 18, 5477 27 of 28

optimized considering the wide operation ranges, rather than only focusing on high torque density at singular operation point.

Author Contributions: Conceptualization, Z.-Q.Z. and S.W.; methodology, S.W. and Z.-Q.Z.; software, S.W.; validation, S.W., Y.X., and Z.-Q.Z.; formal analysis, S.W. and Z.-Q.Z.; investigation, S.W. and Z.-Q.Z.; resources, Z.-Q.Z.; data curation, S.W.; writing—original draft preparation, S.W.; writing—review and editing, Z.-Q.Z., Y.X., and D.L.; visualization, S.W.; supervision, Z.-Q.Z.; project administration, Z.-Q.Z.; funding acquisition, Z.-Q.Z. All authors have read and agreed to the published version of the manuscript.

Funding: This research was funded by the Midea Industrial Technology Business group, grant number: R/157532-11-1.

Data Availability Statement: The original contributions presented in the study are included in the article, further inquiries can be directed to the corresponding author.

Conflicts of Interest: The authors declare no conflicts of interest.

References

- 1. Gadiyar, N.; Van de Ven, J.; Severson, E.L. Evaluation of torque-dense electric machine technology for off-highway vehicle electrification. *IEEE Trans. Ind. Appl.* **2024**, *60*, 3062–3074. [CrossRef]
- Levi, E. Multiphase electric machines for variable-speed applications. IEEE Trans. Ind. Electron. 2008, 55, 1893–1909. [CrossRef]
- 3. Cao, W.P.; Mecrow, B.C.; Atkinson, G.J.; Bennett, J.W.; Atkinson, D.J. Overview of electric motor technologies used for more electric aircraft (MEA). *IEEE Trans. Ind. Electron.* **2012**, *59*, 3523–3531.
- 4. Barcaro, M.; Bianchi, N.; Magnussen, F. Six-phase supply feasibility using a PM fractional-slot dual winding machine. *IEEE Trans. Ind. Appl.* **2011**, 47, 2042–2050. [CrossRef]
- 5. Barcaro, M.; Bianchi, N.; Magnussen, F. Faulty operations of a PM fractional-slot machine with a dual three-phase winding. *IEEE Trans. Ind. Electron.* **2011**, *58*, 3825–3832. [CrossRef]
- 6. Abdel-Khalik, A.S.; Ahmed, S.; Massoud, A.M. Low space harmonics cancellation in double layer fractional slot winding using dual multi-phase winding. *IEEE Trans. Magn.* **2015**, *51*, 8104710. [CrossRef]
- 7. Abdel-Khalik, A.S.; Ahmed, S.; Massoud, A.M. A six-phase 24 slot-10 pole permanent-magnet machine with low space harmonics for electric vehicle applications. *IEEE Trans.* **2016**, *52*, 8700110. [CrossRef]
- 8. Demir, Y.; Aydin, M. A novel dual three-phase permanent magnet synchronous motor with asymmetric stator winding. *IEEE Trans. Magn.* **2016**, *52*, 8105005. [CrossRef]
- 9. Zheng, P.; Wu, F.; Lei, Y.; Sui, Y.; Yu, B. Investigation of a novel 24slot/14-pole six-phase fault-tolerant modular permanent-magnet in-wheel motor for electric vehicles. *Energies* 2013, *6*, 4980–5002. [CrossRef]
- 10. Barcaro, M.; Bianchi, N.; Magnussen, F. Analysis and tests of a dual three-phase 12-slot 10-pole permanent-magnet motor. *IEEE Trans. Ind. Appl.* **2010**, *46*, 2355–2362. [CrossRef]
- 11. Cheng, L.; Sui, Y.; Zheng, P.; Yin, Z.; Wang, C. Influence of stator MMF harmonics on the utilization of reluctance torque in six-phase PMA-SynRM with FSCW. *Energies* **2018**, *11*, 108. [CrossRef]
- 12. Zhu, S.; Cox, T.; Xu, Z.; Gerada, C. Novel 24-slots14-poles fractional-slot concentrated winding topology with low-space harmonics for electrical machine. *J. Eng.* **2019**, 2019, 3784–3788. [CrossRef]
- 13. Patel, V.I.; Wang, J.; Wang, W.; Chen, X. Six-phase fractional-slot-perpole-per-phase permanent-magnet machines with low space harmonics for electric vehicle application. *IEEE Trans. Ind. Appl.* **2014**, *50*, 2554–2563. [CrossRef]
- 14. Zhao, W.; Zhao, F.; Lipo, T.A.; Kwon, B.-I. Optimal design of a novel V-type interior permanent magnet motor with assisted barriers for the improvement of torque characteristics. *IEEE Trans. Magn.* **2014**, *50*, 8104504. [CrossRef]
- 15. Zhao, W.; Chen, D.; Lipo, T.A.; Kwon, B. Performance improvement of ferrite-assisted synchronous reluctance machines using asymmetrical rotor configurations. *IEEE Trans. Magn.* **2015**, *51*, 8108504. [CrossRef]
- 16. Xing, F.; Zhao, W.; Kwon, B.I. Design and optimisation of a novel asymmetric rotor structure for a PM-assisted synchronous reluctance machine. *IET Electr. Power Appl.* **2018**, *13*, 573–580. [CrossRef]
- 17. Yang, H.; Mao, Y.; Lyu, S.; Lin, H.; Chen, Z.; Zhan, H.; Liu, C. Investigation on operating characteristics of asymmetric-magnetic-pole interior permanent magnet machines under maximum torque per ampere control. *IEEE Trans. Ind. Electron.* **2024**, 72, 177–187. [CrossRef]
- 18. Xu, M.; Zhao, W.; Ji, J.; Chen, Q.; Liu, G. Auxiliary notching rotor design to minimize torque ripple for interior permanent magnet machines. *IEEE Trans. Ind. Electron.* **2024**, *71*, 12051–12062. [CrossRef]

Energies **2025**, 18, 5477 28 of 28

19. Zhao, W.; Lipo, T.A.; Kwon, B.-I. Optimal design of a novel asymmetrical rotor structure to obtain torque and efficiency improvement in surface inset PM motors. *IEEE Trans. Magn.* **2015**, *51*, 8100704. [CrossRef]

- 20. Alsawalhi, J.Y.; Sudhoff, S.D. Design optimization of asymmetric salient permanent magnet synchronous machines. *IEEE Trans. Energy Convers.* **2016**, *31*, 1315–1324. [CrossRef]
- 21. Zhao, W.; Xing, F.; Wang, X.; Lipo, T.A. Design and analysis of a novel PM-assisted synchronous reluctance machine with axially integrated magnets by the finite-element method. *IEEE Trans. Magn.* **2017**, *53*, 8104104. [CrossRef]
- 22. Zhao, W.; Shen, H.; Lipo, T.A.; Wang, X. A new hybrid permanent magnet synchronous reluctance machine with axially sandwiched magnets for performance improvement. *IEEE Trans. Energy Convers.* **2018**, *33*, 2018–2029. [CrossRef]
- 23. Liu, G.; Xu, G.; Zhao, W.; Du, X.; Chen, Q. Improvement of torque capability of permanent-magnet motor by using hybrid rotor configuration. *IEEE Trans. Energy Convers.* **2017**, *32*, 953–962. [CrossRef]
- 24. Zeng, X.; Quan, L.; Zhu, X.; Xu, L.; Liu, F. Investigation of an asymmetrical rotor hybrid permanent magnet motor for approaching maximum output torque. *IEEE Trans. Appl. Supercond.* **2019**, *29*, 0602704. [CrossRef]
- 25. Xiao, Y.; Zhu, Z.Q.; Jewell, G.W.; Chen, J.T.; Wu, D.; Gong, L.M. A novel asymmetric interior permanent magnet synchronous machine. *IEEE Trans. Ind. Appl.* **2022**, *58*, 3370–3382. [CrossRef]
- 26. Xiao, Y.; Zhu, Z.Q.; Jewell, G.W.; Chen, J.; Wu, D.; Gong, L. A novel spoke-type asymmetric rotor interior permanent magnet machine. *IEEE Trans. Ind. Appl.* **2021**, *57*, 4840–4851. [CrossRef]
- 27. Xiao, Y.; Wang, R.; Ji, B.; Ma, Y.; Zhu, Z.Q. A novel dual-layer asymmetric interior permanent magnet machine with high torque density and low torque ripple. In Proceedings of the 2024 Third International Conference on Sustainable Mobility Applications, Renewables and Technology (SMART), Dubai, United Arab Emirates, 22–24 November 2024; pp. 1–7.
- 28. Huang, J.; Fu, W.; Niu, S.; Zhao, X.; Bi, Y.; Qiao, Z. A novel spoke-type asymmetric rotor interior permanent magnet machine. *Energies* **2022**, *15*, 9385. [CrossRef]
- 29. Li, S.; Di, C.; Bao, X. A novel asymmetric interior permanent magnet machine with auxiliary flux barriers. *IEEJ Trans. Electr. Electron. Eng.* **2024**, *19*, 1263–1274. [CrossRef]
- 30. Li, S.; Wang, L.; Bao, X. A asymmetric rotor interior permanent magnet mechanical design considering operating conditions. *Electr. Eng.* **2025**, 107, 10363–10377. [CrossRef]
- 31. Burress, T.A.; Campbell, S.L.; Coomer, C.L. Evaluation of the 2010 Toyota Prius Hybrid Synergy Drive System; Oak Ridge Nat. Lab., U.S. Dept. Energy: Oak Ridge, TN, USA, 2011.
- 32. Wang, S.; Zhu, Z.Q.; Pride, A.; Shi, J.; Deodhar, R.; Umemura, C. Comparison of different winding configurations for dual three-phase interior PM machines in electric vehicles. *World Electr. Veh. J.* **2022**, *13*, 51. [CrossRef]
- 33. Xiao, Y.; Zhu, Z.Q.; Wang, S.S.; Jewell, G.W.; Chen, J.T.; Wu, D.; Gong, L. A novel asymmetric interior permanent magnet machine for electric vehicles. *IEEE Trans. Energy Convers.* **2021**, *36*, 2404–2415. [CrossRef]
- 34. Zhu, Z.-Q.; Xiao, Y. Novel magnetic-field-shifting techniques in asymmetric rotor pole interior PM machines with enhanced torque density. *IEEE Trans. Magn.* **2021**, *58*, 8100610. [CrossRef]
- 35. Chu, W.Q.; Zhu, Z.Q. Average torque separation in permanent magnet synchronous machines using frozen permeability. *IEEE Trans. Magn.* **2013**, 49, 1202–1210. [CrossRef]
- Chen, X.; Wang, J.; Lazari, P.; Chen, L.; Lombard, P. Reluctance torque evaluation for interior permanent magnet machines using frozen permeability. In Proceedings of the International Conference on Power Electronics, Machines and Drives (PEMD), Manchester, UK, 8–10 April 2014.
- 37. Wang, S.; Zhu, Z.Q.; Pride, A.; Deodhar, R.; Umemura, C. Torque separation for dual three-phase PM machines using frozen permeability method. In Proceedings of the International Conference on Power Electronics, Machines and Drives (PEMD), Nottingham, UK, 15–17 December 2020.
- 38. Chu, W.Q.; Zhu, Z.Q.; Zhang, J.; Liu, X.; Stone, D.A.; Foster, M.P. Investigation on operational envelops and efficiency maps of electrically excited machines for electrical vehicle applications. *IEEE Trans. Magn.* **2015**, *51*, 8103510. [CrossRef]
- Hsu, J.S.; Ayers, C.W.; Coomer, C.L.; Wiles, R.H.; Campbell, S.L.; Lowe, K.T.; Michelhaugh, R.T. Report on Toyota/Prius Motor torque-Capability, Torque-Property, No-Load Back EMF, and Mechanical Losses; Oak Ridge Nat. Lab., U.S. Dept. Energy: Oak Ridge, TN, USA, 2004.
- 40. Zhu, Z.Q. A simple method for measuring cogging torque in permanent magnet machines. In Proceedings of the IEEE Power & Energy Society General Meeting, Calgary, AB, Canada, 26–30 July 2009; pp. 1–4.

Disclaimer/Publisher's Note: The statements, opinions and data contained in all publications are solely those of the individual author(s) and contributor(s) and not of MDPI and/or the editor(s). MDPI and/or the editor(s) disclaim responsibility for any injury to people or property resulting from any ideas, methods, instructions or products referred to in the content.